GEOLOGICA CARPATHICA, DECEMBER 2021, 72, 6, 461–481 https://doi.org/10.31577/GeolCarp.72.6.2

Upper Neoproterozoic garnet-bearing granites in the Zeber-Kuh region from east central Iran micro plate: Implications for the magmatic evolution in the northern margin of Gondwanaland

HABIB MOLLAI[1,✉], RAHIM DABIRI[1], HABIB ALLAH TORSHIZIAN[1], GEORGIA PE-PIPER[2] and WEI WANG[3]

[1]Department of Geology, Mashhad Branch, Islamic Azad University, Mashhad, Iran; ✉Mollai@mshdiau.ac.ir
[2]Department of Geology, Saint Mary's University, Halifax, N.S., B3H 3C3, Canada; gpiper@smu.ca
[3]State Key Laboratory of Geological Processes and Mineral Resources, School of Earth Sciences, China University of Geosciences, Wuhan, Hubei Province, P.R. China

(Manuscript received December 28, 2020; accepted in revised form November 11, 2021; Associate Editor: Igor Petrik)

Abstract: This paper reports, for the first time, on a garnet-bearing granite body at Zeber-Kuh and interprets its petrogenesis, age and tectonic setting within the context of the evolution of the Cadomian subduction system. The primary minerals imply an origin at pressures greater than 8–6 kbars (~25 km depth) and at temperatures above 700 °C with >10 % water. The Zeber-Kuh granite is in tectonic contact with neighboring rocks. This igneous body has average SiO_2 of 71 wt. %, average Al_2O_3 of 14 wt. %, 3.1–3.6 wt. % Na_2O, 3.0–6.2 wt. % K_2O and 3.3–0.1 wt. % MgO. The granite is characterized by light rare earth element (LREE)-enrichment, relatively flat heavy rare earth element (HREE) patterns with a small negative Eu anomaly and moderately fractioned REE patterns [average $(La/Yb)_N$=11.32]. Decreasing Fe_2O_{3T}, MgO, CaO, TiO_2, Ba, Eu and Sr with increasing SiO_2 contents are consistent with fractional crystallization and can be related to fractionation of plagioclase, clinopyroxene, hornblende, and apatite. Two granite samples yielded U–Pb zircon ages of 533±3 and 534±6 Ma, which regionally correspond to the younger Cadomian magmatism. Cathodoluminescence images of zircon grains from the studied samples show well-developed oscillatory bands, typical of felsic magmas zircons, and Th/U ratios range from 0.79 to 0.45 with an average of 0.60. The REE patterns of the zircons show progressive enrichment from LREE to HREE with a positive Ce anomaly and a negative Eu anomaly.The garnet-bearing granite of Zeber-Kuh represents the final stage of Cadomian magmatism along an extensional continental arc adjacent to the northern active margin of Gondwanaland.

Keywords: East-Central Iran, garnet-bearing granite, U–Pb geochronology, geochemistry, Zeber-Kuh.

Introduction

The Central Iranian micro-continent (Fig. 1) exposes a detailed record of late Neoproterozoic to early Cambrian (Cadomian) syn-tectonic magmatism. Widespread Cadomian rocks in Iran and Turkey represent fragments of continental arcs that formed during subduction at the northern active margin of Gondwana. The rocks form part of a 100 million-year-long phase of arc and back-arc magmatism in Iran and Turkey, represented by radiometric ages between 522 and 619 Ma (Horton et al. 2008; Romer et al. 2010).

The Cadomian magmatic rocks of the Kuh-e-Sarhangi region (Table 1, Fig. 1a), including the Lakhbargheshi and Deh Zaman plutons, the Yakhab granitoid and the Tapeh-Tagh Granitic Gneiss were studied by Mollai et al. (2014) and Rossetti et al. (2015). They include unusual biotite granites with magmatic epidote and garnet, indicating emplacement under high-pressure conditions (Zen 1985).

World-wide, garnet-bearing granites are widespread and have multiple origins. Most occur in S-type granites, derived from partial melting of metasedimentary crustal rocks. However, a few have an origin in I-type granites, derived from igneous sources above subduction zones (Chappell & White 1992) and others are reported from A-type granites, formed in back-arc or anorogenic environments (Grebennikov 2014; El Bahariya 2021). Although some garnets in granites are xenocrystic, most are of magmatic origin. The presence of magmatic garnet and epidote is indicative of water-rich magmas at high pressures and relatively low temperatures (Schmidt & Poli 2004).

The Zeber-Kuh study area in the Kuh-e-Sarhangi region (Fig. 1b) is located north of the Lut Block and is bounded by two large Cenozoic strike-slip fault zones, the Dorouneh Fault to the north and the Great Kavir Fault to the south. We report here the U–Pb Concordia ages on zircon by laser ablation inductively coupled plasma mass spectrometry, major and trace elements of bulk rocks, and field observations from the upper Neoproterozoic rocks of the Zeber-Kuh garnet-bearing granite from Ozbak Kuh map (Ruttner et al. 1970). To provide context for this study, we also compile all geochemistry and geotectonic information from the central and northeastern Iranian Cadomian terrains and use these data to

(cc) BY-NC-ND

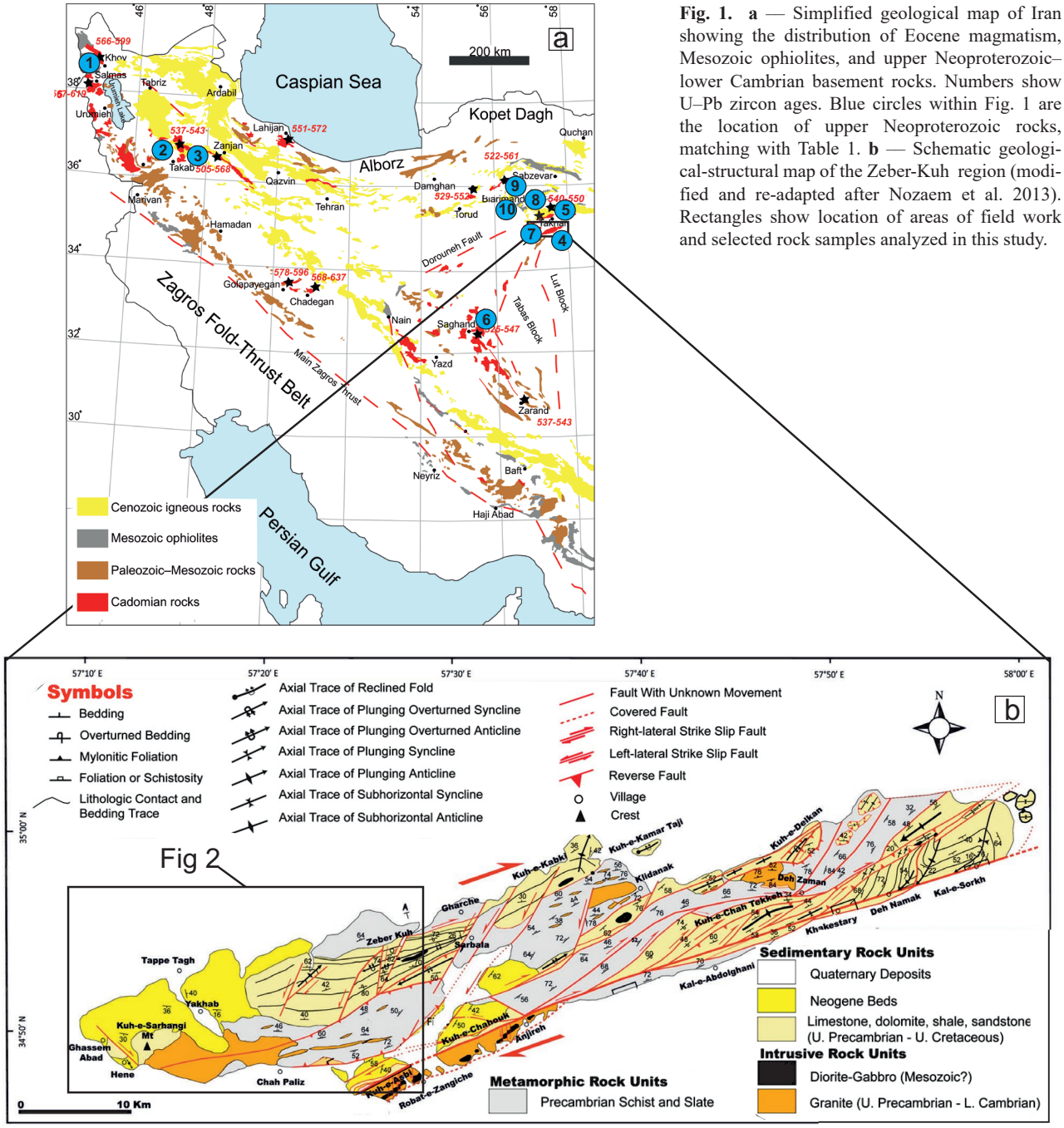

Fig. 1. **a** — Simplified geological map of Iran showing the distribution of Eocene magmatism, Mesozoic ophiolites, and upper Neoproterozoic–lower Cambrian basement rocks. Numbers show U–Pb zircon ages. Blue circles within Fig. 1 are the location of upper Neoproterozoic rocks, matching with Table 1. **b** — Schematic geological-structural map of the Zeber-Kuh region (modified and re-adapted after Nozaem et al. 2013). Rectangles show location of areas of field work and selected rock samples analyzed in this study.

better understand the late Neoproterozoic arc magma formation in east-central Iran. The purpose of this research is to present new in-situ U–Pb geochronology, geochemistry and petrology of the Zeber-Kuh garnet granite rocks.

Geological setting

Regional geology of Cadomian magmatism

Both Iranian and Arabian basements show that stabilization occurred in the late Proterozoic to early Cambrian at the margin of Gondwana (Ghorbani 2013), with cratonization of Iran resulting from the Pan-African orogeny (Duchmand-Zadeh 1969; Etemad-Saeed et al. 2016). The oldest sedimentary rocks in Iran are the siliciclastic Kahar Formation, which based on paleontology and stratigraphic studies may be as old as 800 Ma, with the uppermost layers showing an age of about 650 Ma (Duchmand-Zadeh 1969; Poursoltani & Hrati Sabzvar 2019; Jamshidibadr et al. 2020). The oldest radiometrically dated rocks in Iran are as old as 900 Ma (Hushmandzadeh, Geological Survey of Iran unpublished report). The best known Precambrian sedimentary rocks are Kahar and Ghareh-dash formations and the lower part of the Soltanieh Formation

in North and Central Iran. Magmatic rocks with an age of 630–530 Ma have been reported from Central Iran and Azerbaijan and are related to the Pan-African tectonic-magmatic episode (Ramezani & Tucker 2003; Dabiri et al. 2018). Based on field observations, an older age has been suggested for some metamorphic units in Central Iran like Robat Poshtebadam, Saghand, and Mahneshan in Azerbaijan (Haghipour 1974; Alavi 1994). Different ages of the upper Neoproterozoic magmatic rocks of ~515 and 630 Ma have been reported in different regions of Iran (Table 1 and Fig. 1) and include Central Iran (Kuh-e-Sarhangi region; Born award–Bardaskan–Taknar Zone in the Saghand Region; Tapeh-Tagh and the Biarjmand-Torud region, along with a region near Kashmar, Delbar, Zeber-Kuh and the Yakhab region of east-central Iran) and the Northwest and West of Iran (Khoy-Salmas, Soursat, Sanandaj-Sirjan and Zanjan-Takab). The areas of Neoproterozoic basement rocks constitute the Central Iranian microcontinent, which is bounded by fold and thrust belts of the Alpine–Himalayan Orogeny that lie between the Eurasian plate in the northeast and the Arabian plate in the southwest. It comprises a peri-Gondwanan active continental margin that rifted from Gondwana in the Devonian and accreted to Eurasia in the Triassic Cimmerian orogeny (Metcalfe 2013; Zanchi et al. 2015; Moghadam et al. 2016; Tarabi et al. 2019; Kumar & Pandit 2020; Saeidi et al. 2020).

Kashmar–Kerman Tectonic Zone

The Lut, Tabas and Yazd blocks (Fig. 1a) are the main crustal blocks of the Central Iranian micro-continent in Central Iran (Soffel et al. 1996; Jahangiri 2007; Shahabpour 2007). The Yazd and Tabas blocks are separated by the Kashmar–Kerman zone, which exposes deeper parts of the Cadomian basement (Ramezani & Tucker 2003). The study area is located in the northern part of of this zon and is cut by the NE–SW trending Great Kavir and Dorouneh upper Cenozoic strike-slip faults. The arcuate sinistral Dorouneh Fault is commonly regarded as the longest intraplate strike-slip fault of Central Iran, extending between longitudes 54°E and 60°30'E, with an along-strike cumulative length in excess of 750 km (Tadayon et al. 2017). The architecture of the Dorouneh Fault is characterized by three main fault strands, western, central, and eastern, respectively (Javadi et al. 2013). The western strand, also known as Great Kavir Fault, extends from Dorouneh village to central Iran for a cumulative length of approximately 500 km, striking NE–SW and showing sinistral kinematics (Javadi et al. 2013). The Dorouneh Fault varies along its curvature from purely strike slip in the west to transpression in the east and experienced latest Neogene (Mio–Pliocene) slip sense inversion from dextral to sinistral along much of the fault trace (Javadi et al. 2015). Thus

Table 1: Geological characteristics of some of the Neoproterozoic magmatic rocks in Iran.

Area	No.	Region	Age (Ma)	Rock types	Geotectonic setting	Geochemical characteristics	References
North West Iran	1	Khoy metamorphic complex	550–590	metabasites and metagranites	subduction zone with contamination from recycled sediments	metamorphic conditions of 450–680 °C at 5.5–7.5 kbar	Azizi 2011
	2	Soursat, Sanandaj-Sirjan metamorphic belt	540	S & I-Type granite	syn- to post-collisional	medium-K calc-alkaline to high-K calc-alkaline series	Badr et al. 2013
	3	Zanjan–Takab	~448–562	migmatites and metamorphic rocks	subduction-related magmatism of the Urumieh–Dokhtar magmatic belt	includes orthogneiss with migmatite leucosomes and amphibolite	Moghadam et al. 2016
Central Iran	4	Kuh-e-Sarhangi region	575–535	sub-alkaline, dominantly high-K calc-alkaline acidic suite	volcanic arc, subduction-related magmatism within an oblique convergence	high SiO_2 (72.60–77.17 wt. %), and alkalis (up to 8 wt. %) and low Mg# (7–35 wt. %)	Rosetti et al. 2015
	5	Born award - Bardaskan-Taknar -Zone	540–550	S & I-Type granite	crustal contamination (S-type granite)	middle-high metaluminous to low-middle peraluminous; tholeiite, calc-alkaline to high-K calc-alkaline series	Monazzami 2015 ; Karimpour et al. 2011
	6	Saghand Region	from 2400 to 570	island-arc type cratonization	island-arc type cratonization formed the Iranian Precambrian basement	low grade to high grade metamorphic rocks	Nadim 2005
Central East Iran	7	Tapeh-Tagh	520–536	A-type granite	volcanic arc granite (VAG) to the SYN-CoLG	SiO_2 (70.30–79.63 wt. %), lower levels of Fe, Ca, Mg, Ti, P and Sr	Mollai et al. 2019
	8	Delbar Metamorphic-Igneous Complex (Biarjmand region)	542–546	Metamorphic-Igneous Complex	back arc extensional setting in extended continental crust	70–78 wt. % SiO_2, calc-alkaline to high-K calc-alkaline	Balaghi 2014
North East Iran	9	Torud–Biarjmand	560–520	meta-peraluminous S-Type?	continental magmatic arc	arc related calc-alkaline granitic gneiss; high SiO_2, Na_2O; low Fe, Mg and Ca	Moghadam et al. 2016, 2017
North – Central Iran	10	ChahJam–Biarjmand	550–530	granitic–tonalitic gneiss	continental arcs and within plate granite (WPG)	felsic igneous 72.7–73.8 wt.% SiO_2; 0.4–3.3 wt. % K_2O; 3–5.3 wt. % Na_2O	Moghadam et al. 2015

geodetically derived strain rates cannot be extrapolated into the Neogene.

The Kashmar–Kerman Tectonic Zone is a nearly 600 km long, arcuate and structurally complex fault-bounded belt (Rossetti et al. 2015). The Zeber-Kuh and Kuh e Sarhanghi faults are part of the Kashmar–Kerman Tectonic Zone, and form a ~75 km long, sharp fault strand that bounds to the south a NE–SW linear mountain range (Fig. 2). Neoproterozoic igneous and metamorphic rocks crop out within the damage zone of these faults, in association with Paleozoic–Mesozoic cover units in the northern and northwestern parts of Zeber-Kuh and Kuh e Sarhangi (Nozaem et al. 2013; Mollai et al. 2014; Rossetti et al. 2015; Tadayon et al. 2017). The Zeber-Kuh complex is made up of strongly tectonized Precambrian and Paleozoic rocks (Fig. 2) including orthogneiss, garnet–chlorite-amphibolite and mica schists, granitoid plutons (including the Zeber-Kuh, Yakhab, Sarhangi, Robat, Lakhbargheshi and Deh Zaman plutons) (Rossetti et al. 2015) and low grade phyllites (Zeber-Kuh beds) that have been assigned to the Ediacaran (Agard et al. 2005; Mollai et al. 2019). The Zeber-Kuh granite is partly overlain by the Ediacaran to lower Cambrian Soltanieh dolomite and the Paleocene Kerman conglomerate. They are partly covered by Neogene and Quaternary alluvial deposits. Upper Neoproterozoic garnet-bearing granites magmatic rocks of the Yakhab granitoid (Fig. 2) and the Tapeh-Tagh Granitic Gneiss were studied by Mollai et al. (2014). They include unusual biotite granites with magmatic epidote and garnet, indicating emplacement under high-pressure conditions (Zen 1985).

The igneous and metamorphic units, widely exposed in the central part of the region, have been deformed during a Precambrian orogeny and affected by polyphase reactivation during the Mesozoic and Tertiary, with younger brittle deformation events extending to the Quaternary (Nozaem et al. 2013; Rossetti et al. 2015). The overall structural architecture of the pre-Neogene basement succession along the Zeber-Kuh and Kuh e Sarhangi faults is dominated by steeply dipping foliation, folding, and anastomosing fault-bounded tectonic contacts (Nozaem et al. 2013). The U–Pb zircon geochronology indicates that magma was emplaced and crystallized ca. 575–535 Ma, under a tectonic regime with thickened crustal. The Kuh e Sarhangi magmatic belt including Zeber-Kuh exposes the exhumed roots of a volcanic arc. This magmatism is interpreted as part of the Cadomian subduction-related

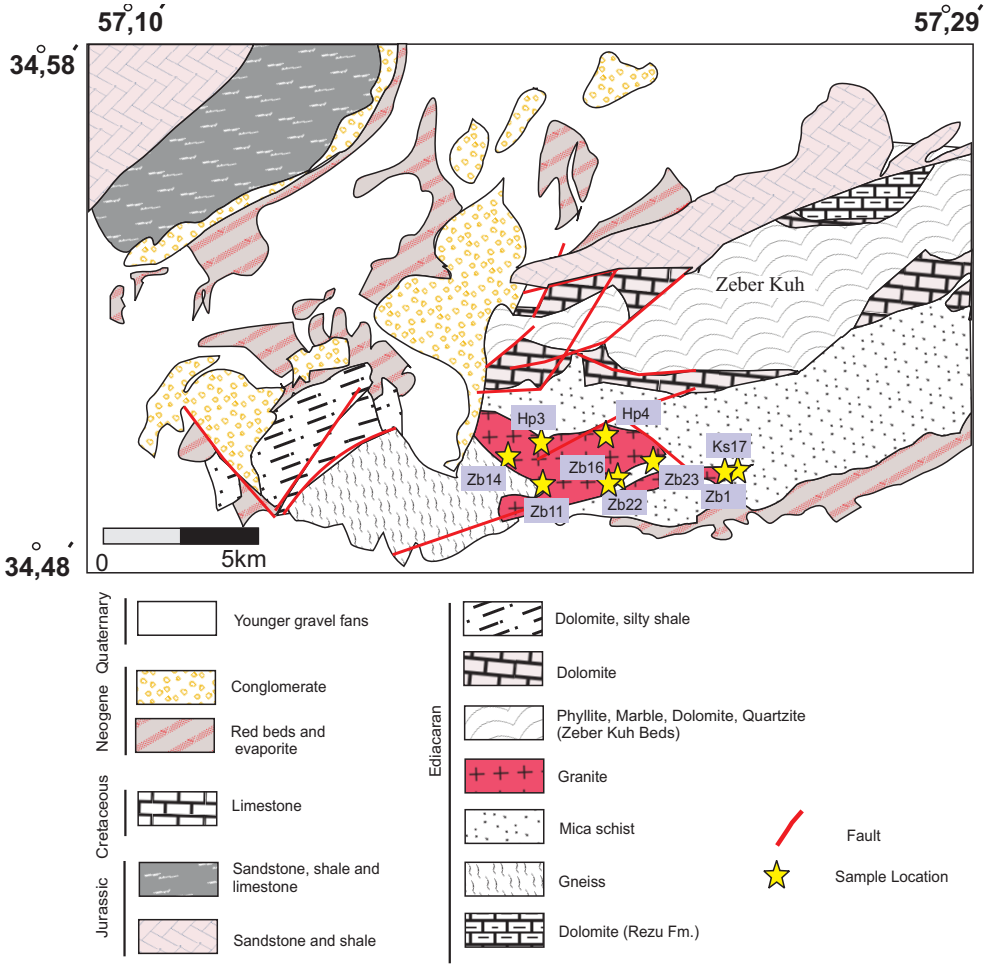

Fig. 2. Geological map of Zeber-Kuh area, with various types of rocks including Cadomian granite, gneiss and sedimentary rocks, along with major and minor faults. Most of the faults strike NE–SW. Modified from the Ozbak Kuh map after Ruttner & Nabavi (1970).

magmatism along the northern margin of Gondwana (Rossetti et al. 2015). The regional Cadomian magmatic flare-up was linked to strong crustal extension above a South-dipping subduction zone beneath northern Gondwana (Rossetti et al. 2015; Moghaddam et al. 2020). Zircon U–Pb–Hf isotopic data indicate derivation of the magmatic protoliths from heterogeneous Proterozoic and upper Archean (0.9–3.6 Ga) crustal components (Nutman et al. 2014).

Zeber-Kuh granite

The Zeber-Kuh garnet-bearing granite pluton that is the focus of this study lies between mica schists and the lower Cambrian Tapeh Tagh granitic orthogneiss complex (Mollai et al. 2019) in the southern portion of the Zeber-Kuh complex. The Zeber-Kuh garnet granite is coarse to medium grained and ranges from pink to dark grey in color (Fig. 3). The grey granite contains micro-diorite enclaves, which increase in abundance eastwards. The majority of the enclaves are dark grey, fine-grained and range in size from a few cm to about 0.5 m. The light grey garnet granite is coarse-grained, mainly contains alkali feldspar, garnet and biotite (Fig. 3b), whereas the dark grey granitoid is very coarse-grained, showing gneissic foliation (Fig. 3c). The granite and granite gneisses nowhere show contact metamorphism with other rocks, but have sharp, in places boudinaged, tectonic contact with mica schist (Fig. 4c).

The cover rocks consist of weakly metamorphosed sequences of shales, limestones, sandstones and Soltanieh dolomites of Ediacaran to early Cambrian age. Soltanieh dolomites in the area are stretched and boudinaged along the main shear contact localized along the boundary with the granite and mica schists, with recrystallization of dolomite and calcite (Fig. 4a). The dolomite is folded on NE–SW axes (Fig. 4d), which are characteristic of the deformation in the area. The Mesozoic sedimentary rocks include marls and limestones (Fig. 4b). Neogene deposits, belonging to the Upper Red Formation and made of alternating Kerman conglomerate, marls, sandstones and evaporites, are uncomformably covered by sub-horizontal Quaternary alluvial deposits. All these deposits mainly strike NE–SW, parallel to the igneous rocks of Zeber-Kuh.

Methods

During field work in 2019, 60 samples were collected, of which three were used for study of zircons and eight for whole-rock geochemistry. Samples for analyses of major and trace elements were powdered in the East Amethyst laboratory in Mashhad, Iran and were then sent to Activation Laboratories, Canada, for inductively coupled plasma mass spectrometry (ICP-MS) according to their Code 4Litho research and Code 4B1 packages, which use lithium metaborate/tetra-

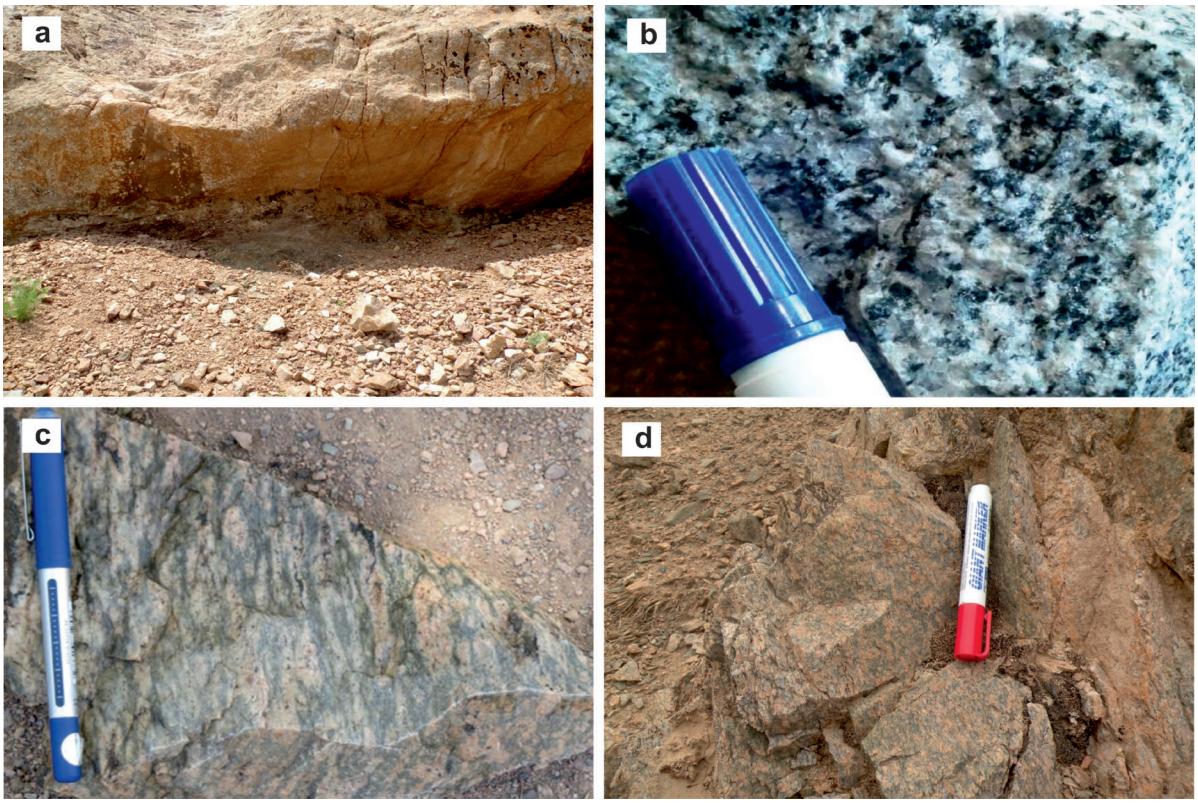

Fig. 3. Various field photos of garnet granitoid rocks in the area under study. a — Pink garnet granitoid showing tectonic contact and tectonic relationship with underlying schist. **b** — Coarse grained light grey garnet granitoid (HP3). **c** — Very coarse grained dark grey granitoid with irregular light and dark banding (HP4). **d** — Medium grained, pinkish, biotite–garnet granitoid (KS17).

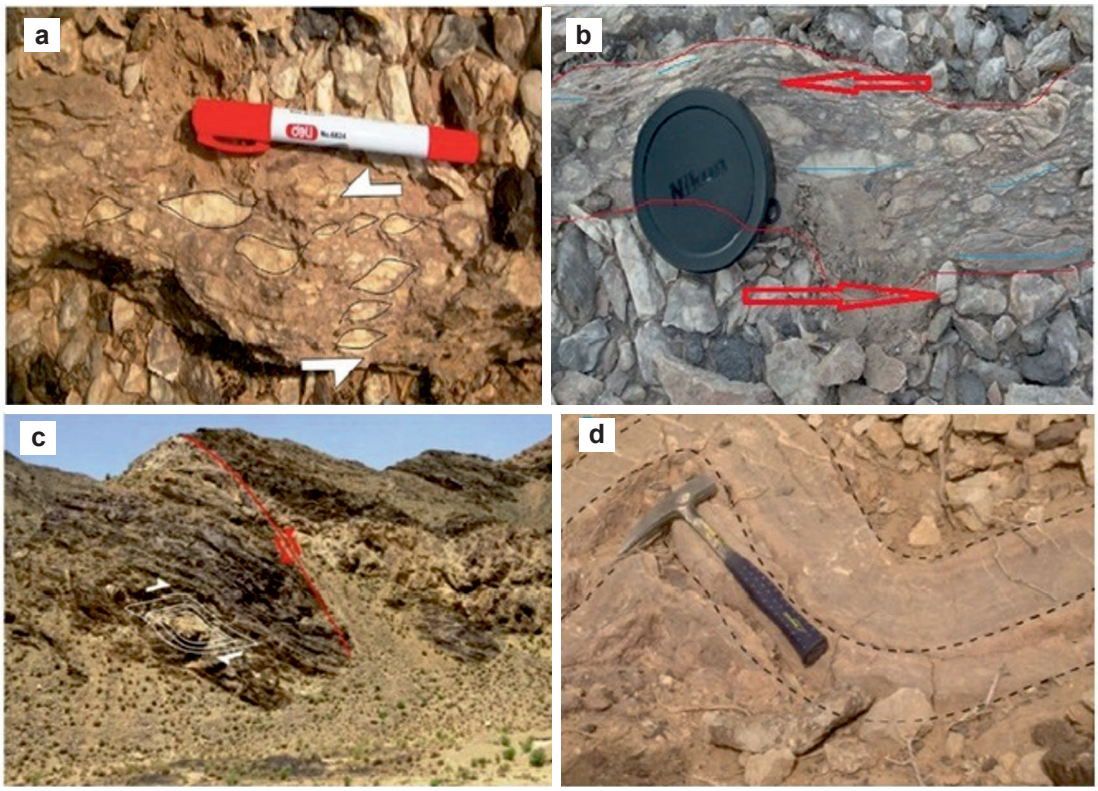

Fig. 4. Field photographs and tectonic activities in the area under study are shown. **a** — Field photograph from the Soltanieh dolomites in the Yakhab area are stretched apart and boudinaged along the main shear contact localized along the boundary of the granite and mica schists. The shear deformation is associated with recrystallization of dolomite and calcite. **b** — Photograph showing sense of shear as deduced from sigma-type calcite and dolomite leading to the formation of a boudinage structure. **c** — Tectonic contact of gneisses with mica schist and formation of boudinage structure along the shear zone. **d** — Folding of Soltanieh dolomite, axis of fold is NE–SW, which is due to compression.

borate fusion. The uncertainty (1σ) is ~2 % for major elements and 5–10 % for trace elements (depending on concentration).

Zircons were separated in the laboratory of the Geological Survey of Iran, using normal methods including sieving, magnetic separation, and floatation. At least fifteen zircon grains per sample were handpicked under a binocular microscope. The zircons were then set in synthetic resin mounts, polished, and cleaned in a warm HNO_3 ultrasonic bath. These zircon grains were sent to the State Key Laboratory of Geological Processes and Mineral Resources (SKLGPM), China University of Geosciences, Wuhan, China. Cathodoluminescence (CL) imaging was carried out using a Gatan Molo Cl4 detector attached to a Zeiss Sigma 300 field emission Scanning Electron Microscope. The CL images are used to characterize any compositional variation within individual zircons during the selection of spot for laser ablation. In situ zircon U–Pb isotope measurements were carried out using a 193 nm ArF Excimer Laser ablation system (GeoLas 2005, Lambda Physik) attached to an Agilent 7500a Inductively coupled plasma mass spectrometer (ICPMS) housed at SKLGPM. The ArF Excimer laser was initially homogenized by a set of beam delivery systems and then focused on the zircon surface with a fluence of 10J/cm^2. Diameter of 32 μm and repetition rate of 5 Hz was employed for 45 seconds as the ablation protocol. The carrier and make-up gas flows were optimized by monitoring ^{238}U intensity during ablating elemental standard NIST610. 2 to 4 mL/min of nitrogen was added to the central gas flow to enhance the sensitivity of U, Th, and Pb isotopes. A "wire" signal smoothing device was applied to improve signal stability. Ratios and absolute abundances of U–Pb isotopes were measured relative to the primary standard 91500, while a secondary standard GJ-1 was analyzed as an unknown sample for quality control. Raw data reduction was performed off-line by using the software ICPMS Data Cal (Yongsheng et al. 2010) and the results are reported at 2σ errors level. Common Pb correction was applied following the method of Andersen (2002) and the differences between common Pb corrected and uncorrected ages were generally small. Concordant plots, TuffZirc Age plots and Probability density plots were processed using the program ISOPLOT (Ludwig 2003).

Petrography and petrology

The garnet-bearing granite samples are leucocratic. The rocks comprise mainly alkali feldspar, quartz, subordinate biotite, garnet, amphibole, plagioclase and accessory muscovite,

epidote and apatite. Some samples have porphyritic textures with hypidiomorphic brown biotite and K-feldspar phenocrysts up to 5 mm. Most samples show equigranular to unequigranular, medium to coarse-grained, consertal textures between biotite and quartz, K-feldspar and plagioclase (albite to oligoclase) crystals. These minerals make up the bulk of the rock and are anhedral with slightly interdigitating boundaries.

Sample HP3 (Fig. 5a) has poikilitic texture, with coarse grains mainly made up of anhedral alkali feldspar, garnet, biotite and quartz. The texture of HP3 is typically granitic, ranging from anhedral to subhedral. Sample HP4 (Fig. 5b) is medium grained, mainly containing quartz, biotite, feldspar, and garnet. Sample KS17 has a porphyritic texture, with coarse grained orthoclase, anhedral garnet, quartz and some muscovite (Fig. 5c). The garnet contains small grains of biotite, epidote, and muscovite and in places it forms grain aggregates of up to 2.5 cm in size. The individual garnet grains are usually rimmed by biotite and have no microscopically visible compositional zoning. Garnet shows a close relation with biotite and some of the samples contain muscovite, opaque minerals and epidote as inclusions. Apatite is a common accessory mineral in granitoid rocks of different chemistry and provenance. Apatite is present in the late K-feldspar as small crystals, typically elongate, as long-prismatic zoned crystals and as large xenomorphic unzoned crystals. They are more or less uniform in size and scattered evenly through K-feldspar and lead to a poikilitic texture that resembles sieve texture (Fig. 5d). Alteration products of these rocks include secondary epidote and sericite (Fig. 5e). This section is a medium grains contain hornblende, quartz, orthoclase and calcite. This rock could have been originally a mafic igneous rock (basalt or dolerite) that recrystallized to hornblende (green) and feldspar (colorless) with a banded texture.

Some of the thin sections consist of mainly quartz, orthoclase, and epidote. In the Lakhbargheshi pluton, the primary igneous assemblage is epidote, quartz, and plagioclase (Rossetti et al. 2015). Quartz grains show only minor evidence of strain as indicated by patchy undolose extinction. No primary epidote was observed in the Zeber-Kuh, all of it is considered secondary. The lack of cross-hatched twinning and micro-perthite in the feldspar suggests crystallization in the upper solvus field, and a very low Na content in the magma during the crystallization of these granitoid rocks.

Based on mineral chemistry (Rossetti et al. 2015), feldspars consist of both sodic plagioclase (X_{An}=6–31 %) and alkali feldspar (X_{Ab}=89–99 % and X_{Or}=89–98 %); both perthite (X_{Ab}=28 % X_{Or}=71 %) and antiperthite (X_{Ab}=79 % X_{Or}=20 %) exolution occurs in the alkali feldspar. A phase diagram (*P–T* pseudosection) was calculated for samples Zb1 and Zb22 using the PerpleX software, version 6.9.0 (Connolly 1990, 2005) with the internally consistent thermodynamic dataset hp11ver.dat of Holland & Powell (2011). The bulk rock composition was obtained from the whole rock analysis (Table 2). Calculations were performed in the Na_2O–CaO–K_2O–FeO–MgO–Al_2O_3–SiO_2–H_2O–TiO_2 system, assuming water-saturated conditions and partial melting. Solution models of garnet, white mica, biotite, cordierite (White et al. 2014), sanidine (Thompson & Hovis 1979), and plagioclase (Newton et al. 1980; Newton & Haselton 1981) were used as available from the PerpleX data file. The garnet, as one of the predominant minerals in the area, has compositions broadly corresponding to the almandine – grossular–pyrope – spessartine system ($Alm_{58–70}Grs_{19–31}$ $Prp_{3–9}Sps_{0–13}$), with moderate core-to-rim chemical zonation, characterized by a decrease in the Sps component ana corresponding increase in Alm. Biotite, with a grain size from 0.5 to 3 mm in length, is enriched in TiO_2 (up to 3.0 wt. %) with X_{Mg} ([MgO/(MgO+FeO)]=0.31–0.38). Primary epidote, which is observed in samples Lackh-1 and Y1, occurs mostly as euhedral grains (up to 1 mm in length) adjacent to biotite, in contacts with plagioclase and quartz. Secondary epidote is mostly found as alteration products of igneous plagioclase. Primary epidote has restricted pistacite (Ps, atomic $[Fe^{3+}/(Fe^{3+}+Al^{3+})]$) content between 21 % and 26 %, whereas secondary epidote has lower Ps (17–20 %).

The two pseudosections used a window of 5–20 kbar, 500–950 °C at H_2O saturated conditions and controlled f_{O2} (log f_{O2}=−15). Solidus is at 700 °C, over a pressure interval 5–20 kbar. For sample Zb1, between 600–850 °C, garnet is stable over the whole pressure interval with a maximum of 4–5 vol. % between 13–18 kbar and 650–700 °C. Epidote is stable below 650 °C and above 10 kbar reflecting oxidising conditions on cooling. Sample Zb22 is similar: garnet is stable above 12 kbar at subsolidus temperatures (below 700 °C) and above 8 kbar at magmatic temperatures (>700 °C). The maximum abundance (1–4 vol. %) is above 16 kbar between 650–700 °C. Magmatic (or peritectic) garnet has a maximum (0.4 vol. %) at ~720 °C above 11 kbar. Epidote is stable at subsolidus temperatures, with maximum at 710 °C at 20 kbar and decreases to 500 °C at 5 kbar. In general garnet seems to be both magmatic/peritectic and subsolidus above ca 13 kbar but with a maximum above the solidus at around 750 °C and above 11 kbar for both samples. Epidote is only subsolidus, with maxima above 10 kbar and below 650 °C. For more precise location of intersecting isopleths and for estimating a *P–T* path, it would be necessary to have more precise mineral modes (garnet, biotite, muscovite, plagioclase, epidote) and mineral compositions (garnet, biotite, muscovite, plagioclase). Oxidising conditions are necessary to stabilise epidote: at 8 kbar the controlled log f_{O2} at −15 actually crosses the FMQ buffer at ~780 °C (reducing conditions) and on continued cooling crosses the HM buffer at 600 °C, indicating a shift of the system to oxidation conditions.

The suggested path starting at 780 °C above 8 kbar crosses garnet and ilmenite fields avoiding rutile (Fig. 6). Because epidote is present, the path crosses the solidus at 690 °C and ends in the epidote stability field at ~6 kbar and ~530 °C. Between 6–12 kbar, a small amount of garnet is stable above 680 °C, i.e. is mostly magmatic, as in this interval 90 % of melt is present above 780 °C. Zr saturation for 144 ppm Zr gives T_{sat}=732 °C (Boehnke et al. 2013) or 779 °C (Watson & Harrison 1983). The first temperature corresponds to 60 vol. %

of the melt, the second to 90 vol. %. The pseudosection model predicts K-feldspar (microcline 3–4 vol. %) only as subsolidus below 690 °C at 8 kbars. It is accompanied by small amount of subsolidus muscovite (2 vol. %). Titanite is not stable at reasonable *P–T* conditions in this model and would be crossed only at very low temperatures. The H_2O saturation of the model involves only the water sufficient to stabilize hydrated minerals such as muscovite, epidote and amphibole.

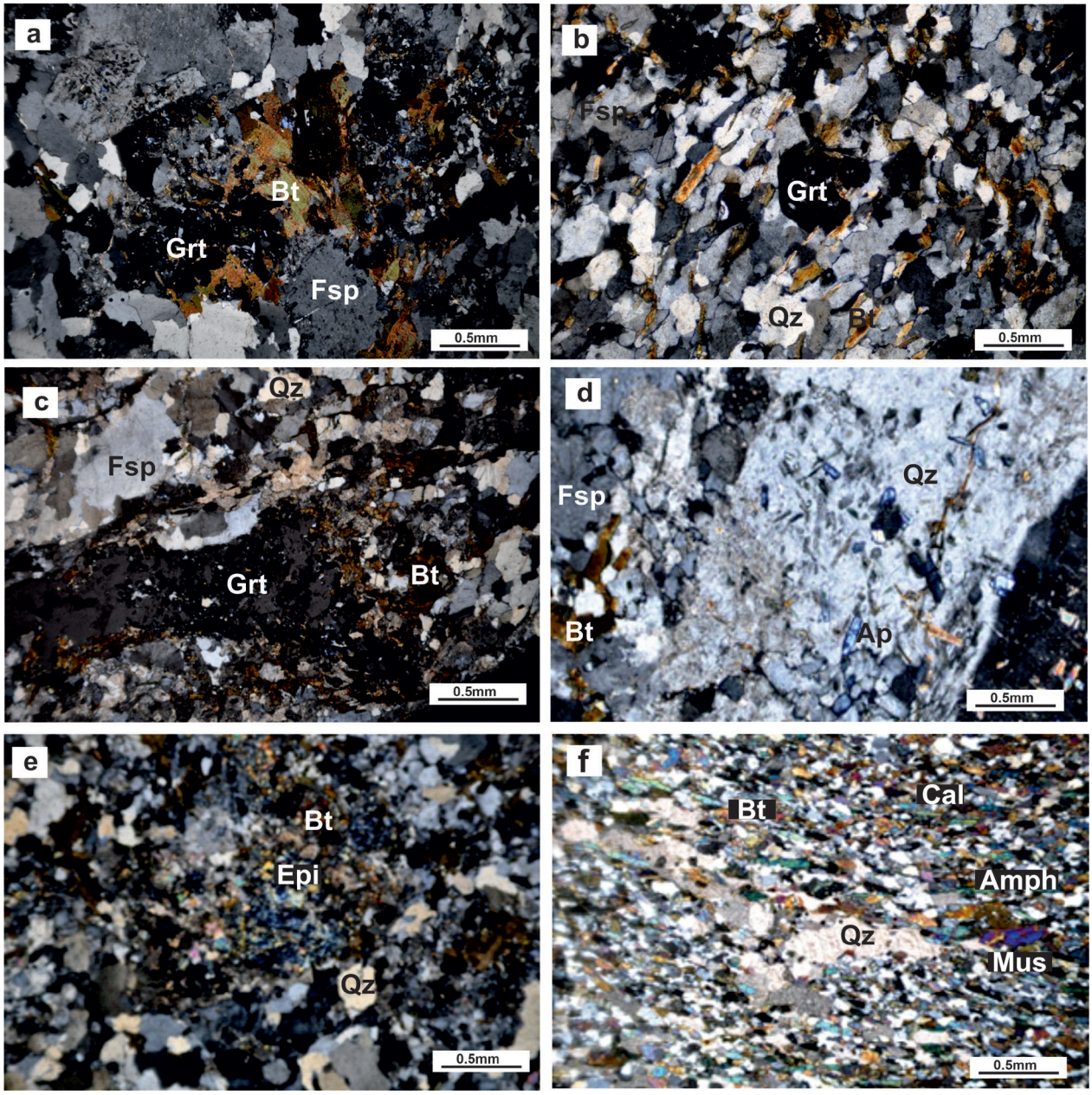

Fig. 5. Microphotographs of various garnet granitoid samples, Zeber-Kuh. **a** — Coarse grained granite with poikilitic texture, mainly made up of anhedral alkali feldspar, garnet, biotite and quartz. The phenocrysts of alkali feldspar and biotite appear replaced by garnet. **b** — Medium grained granite, containing mainly quartz, biotite, feldspar, and garnet. Minerals shows elongation in the lower left portion of section. **c** — Coarse grained granite, containing mainly garnet, biotite, and orthoclase, along with some quartz. Anhedral garnet is embedded in a deformed matrix. **d** — Coarse grained granite with poikilitic texture, containing mainly orthoclase, biotite and apatite, with little quartz. Elongated apatite growth within feldspar phenocrysts. **e** — Medium grained granite with epidote, quartz, garnet and orthoclase, along with some secondary muscovite. Secondary epidote forms by the influence of a fluid phase on calc-silicate rocks as result of hydrothermal alteration. The fluid phase is released in the progressive metamorphism of protoliths which are rich in hydrous minerals. Epidotization is the alteration process in which plagioclase feldspars convert into the epidote group minerals. **f** — Medium grained granite containing amphibole, quartz, orthoclase and calcite. This rock could be originally a mafic igneous rock (basalt or dolerite), metamorphosed to banded hornblende (green) and feldspar (colorless). Abbreviations: Amph=Amphibole; Ap=Apatite; Bt=Biotite; Cal=Calcite; Epi=Epidote Fsp=Feldspar, Grt=garnet; Mus=Muscovite; Qz=quartz.

Table 2: Whole rock geochemical analyses.

Element		Zb1	Zb9*	Zb11*	Zb14	Zb14a	Zb16	altered granite Zb22*	granodiorite Zb23	Detection Limit
SiO_2	%	69.32	69.6	72.31	72.74	72	71.85	74.45	63.67	0.01
Al_2O_3	%	13.76	13.69	12.76	13.26	13.24	13.87	14.15	15.17	0.01
$Fe_2O_{3(T)}$	%	3.38	3.46	3.52	3.21	3.17	3.32	0.91	6.63	0.01
MnO	%	0.06	0.06	0.042	0.027	0.026	0.035	0.009	0.065	0.001
MgO	%	0.76	0.76	0.49	0.47	0.47	0.48	0.11	3.26	0.01
CaO	%	1.3	1.3	1.83	2.14	2.12	1.91	1.19	1.37	0.01
Na_2O	%	3.94	3.99	3.11	3.37	3.37	3.58	6.24	2.96	0.01
K_2O	%	3.79	3.85	3.12	3.15	3.15	2.84	1.01	2.49	0.01
TiO_2	%	0.263	0.265	0.251	0.257	0.256	0.264	0.15	0.796	0.001
P_2O_5	%	0.06	0.05	0.05	0.05	0.06	0.06	0.02	0.18	0.01
LOI	%	1.24	1.23	0.83	1.13	1.18	1.02	1.05	1.72	0.01
Total	%	97.89	98.26	98.34	99.81	99.05	99.23	99.28	98.31	
A/CNK		**1.06**	**1.05**	**1.08**	**1.03**	**1.03**	**1.12**	**1.05**	**1.51**	
A/NK		**1.30**	**1.28**	**1.50**	**1.48**	**1.48**	**1.55**	**1.25**	**2.01**	
K_2O/ Na_2O		**0.96**	**0.96**	**1.00**	**0.93**	**0.93**	**0.79**	**0.16**	**0.84**	
Ba/Sr		**6.5**	**6.7**	**4.9**	**4.4**	**4.3**	**6.2**	**2.9**	**3.0**	
Sc	ppm	11	11	10	10	10	11	16	17	1
Be	ppm	2	2	2	2	2	2	2	3	1
V	ppm	24	23	21	19	21	21	14	136	5
Cr	ppm	< 20	< 20	30	40	30	< 20	< 20	90	20
Co	ppm	4	4	4	4	4	4	< 1	19	1
Ni	ppm	4	5	5	6	4	4	5	47	1
Cu	ppm	14	12	11	5	6	3	69	28	1
Zn	ppm	546	508	49	45	22	43	7	70	1
Cd	ppm	< 0.5	0.5	< 0.5	< 0.5	< 0.5	< 0.5	< 0.5	< 0.5	0.5
S	%	0.015	0.01	0.008	0.009	0.006	0.008	0.01	0.008	0.001
Ga	ppm	19	17	15	15	16	16	13	20	1
Ge	ppm	2.5	2.5	2	1.9	2	1.6	1.3	1.6	0.5
As	ppm	< 5	< 5	< 5	< 5	< 5	< 5	< 5	< 5	5
Rb	ppm	118	116	98	98	96	85	26	87	1
Sr	ppm	123	123	125	152	156	142	109	214	2
Y	ppm	23.6	25.8	22.2	23.3	22.6	25	25.5	29.3	0.5
Zr	ppm	115	119	124	119	123	119	144	175	1
Nb	ppm	6.1	5.4	5.9	5.5	5.7	5.7	7.4	9.9	0.2
Mo	ppm	< 2	< 2	< 2	< 2	< 2	< 2	< 2	< 2	2
Ag	ppm	< 0.3	< 0.3	< 0.3	< 0.3	< 0.3	< 0.3	< 0.3	< 0.3	0.3
In	ppm	< 0.1	< 0.1	< 0.1	< 0.1	< 0.1	< 0.1	< 0.1	< 0.1	0.1
Sn	ppm	2	2	3	3	3	3	2	3	1
Sb	ppm	< 0.2	< 0.2	0.3	0.4	0.3	< 0.2	0.3	0.4	0.2
Cs	ppm	2.8	2.5	4.2	3.9	3.9	5.1	0.4	3.2	0.1
Ba	ppm	805	820	616	675	675	880	316	640	3
La	ppm	28.30	27.40	23.00	25.00	25.30	22.90	30.40	38.30	0.05
Ce	ppm	4.16	52.60	44.00	48.70	49.10	46.30	57.50	76.90	0.05
Pr	ppm	5.81	5.79	4.85	5.30	5.41	5.18	6.41	8.71	0.01
Nd	ppm	22.1	20.6	16.6	18.3	19.1	19.4	22.9	32.1	0.05
Sm	ppm	4.42	4.64	3.42	4.03	4.06	4.55	4.91	6.95	0.01
Eu	ppm	0.892	0.857	0.625	0.692	0.725	0.707	0.546	1.42	0.005
Gd	ppm	4.1	4.01	3.24	3.62	3.56	4.08	4.31	5.93	0.01
Tb	ppm	0.71	0.68	0.56	0.62	0.63	0.68	0.73	0.92	0.01
Dy	ppm	4.33	4.25	3.49	3.82	3.77	4.05	4.33	5.37	0.01
Ho	ppm	0.9	0.87	0.72	0.8	0.78	0.83	0.88	1.07	0.01
Er	ppm	2.67	2.63	2.15	2.41	2.31	2.46	2.65	3.06	0.01
Tm	ppm	0.406	0.399	0.33	0.367	0.354	0.373	0.396	0.455	0.005
Yb	ppm	2.76/	2.75	2.33	2.57	2.49	2.52	2.69	3	0.01
Lu	ppm	0.461	0.444	0.41	0.425	0.424	0.42	0.442	0.484	0.002
Hf	ppm	3.4	3.2	3.5	3.2	3.3	3.2	4	4.3	0.1
Ta	ppm	0.54	0.51	0.55	0.52	0.5	0.58	0.73	0.79	0.01
W	ppm	< 0.5	< 0.5	0.9	< 0.5	1.1	< 0.5	0.7	0.9	0.5
Tl	ppm	0.63	0.62	0.46	0.41	0.44	0.39	0.18	0.51	0.05
Pb	ppm	114	107	18	8	5	18	< 3	< 3	3
Bi	ppm	< 0.1	0.3	< 0.1	< 0.1	< 0.1	< 0.1	< 0.1	1	0.1
Th	ppm	10.4	9.38	9.18	9.95	9.62	9.89	12.5	10.1	0.05
U	ppm	2.07	2.2	1.9	1.89	1.88	2.43	2.3	2.15	0.01

* indicates magmatic garnet

Analyses by ICPMS at Activation Laboratories, Canada, according to their Code 4Lithoresearch and Code 4B1 packages, which use lithium metaborate/tetraborate fusion.

The amount of H_2O rises from 1 wt. % at 550 °C to 11 wt. % in the melt at 780 °C.

Comparison can be made with the rocks from the Skibotn Nappe Complex of the Scandinavian Caledonides, which show a mineral assemblage of garnet+plagioclase+biotite+whitemica+kyanite+rutile ±K-feldspar±sillimanite. Thermo-dynamic modelling suggested (Ziemniak et al. 2019) that garnet was stable at *P–T* conditions of ~680–720 °C and ~8–10 kbars in the stability field of kyanite and the rocks underwent partial melting during exhumation following a clockwise *P–T* path. A second episode highlighted by growth of secondary white mica resulted from subsequent overprint in amphibolite and greenschist facies. The *P–T* path suggested for the minerals in the Zeber-Kuh granite (Fig. 6) is close to isobaric cooling. The path is hypothetical, and dependant on assumptions of H_2O saturated conditions and moderate oxygen fugacity (log f_{O2}=−15). Relatively low Zr T_{sat} imply that zircon in Zb22 should be fully magmatic. This interpretation is supported by the euhedral to subhedral, elongated or equant prismatic shape of most zircon grains, with the presence of oscillatory zoning. Most of zircon grains have high Th/U ratios ranges between 0.79–0.45 with an average of 0.60.

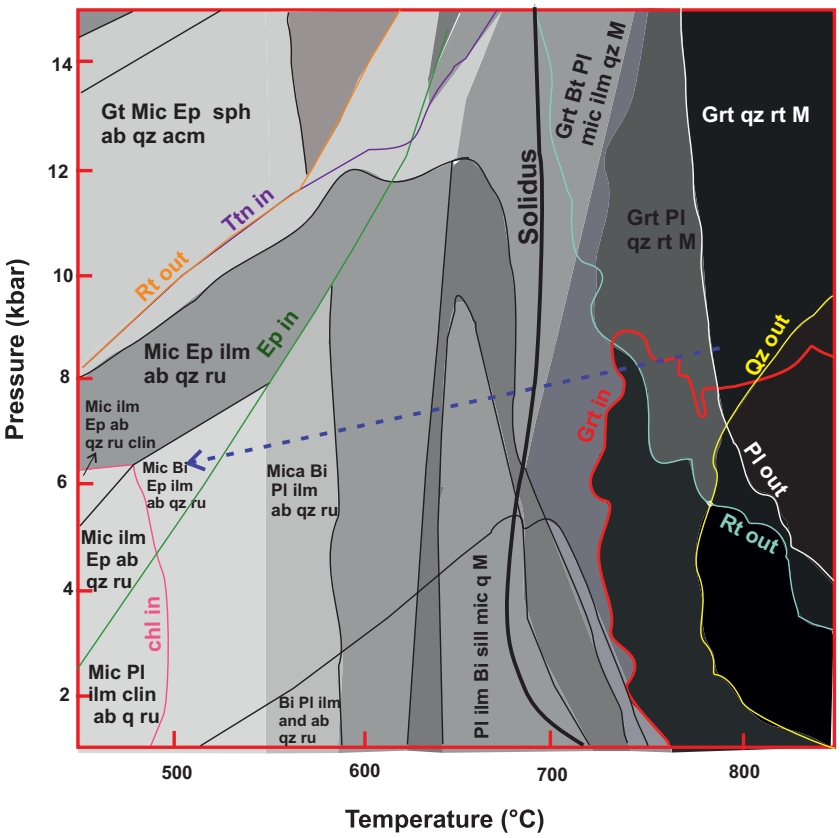

Fig. 6. *P–T* pseudosection of the Zeber-Kuh garnet granite calculated at H_2O saturated conditions and oxygen fugacity controlled at log f_{O2}=−15. Phase boundaries for Grt, Qz, Rt, Ttn, Ep and Chl are shown along with suggested *P–T* path (blue dashed line).

Geochemistry

Out of sixty samples, eight representative samples of garnet granite were analyzed for major and trace elements (Table 2). Seven of the samples are granites, with 69–74.5 wt. % SiO_2 and one is a granodiorite with 63.8 wt. % SiO_2 (Fig. 7a). The range of other major elements in these rocks is 12.8–15.0 wt. % Al_2O_3 (average 14 wt. %); 3.1–3.6 wt. % Na_2O; 3.0–6.2 wt. % K_2O; 0.1–3.3 wt. % MgO; 0.8–0.15 wt. %.TiO_2 and low concentrations of P_2O_5 (0.02–0.2 wt. %), despite the common apatite in thin section. Comparing the Zeber-Kuh granite with geochemical data of the I-type granite in the Lakhbargheshi area (Rossetti et al. 2015), the Lakhbargheshi granite shows higher SiO_2 and K_2O (average 74.7 wt. % and 4.9 wt. % respectively) but lower Al_2O_3 and N_2O (average 12.3 wt. % and 2.8 wt. % respectively) and both granites contain low Fe_2O_3, MgO and CaO. The most silicic granite sample (Zb22) appears altered, with very high Na/K ratio. It also shows high values of Al_2O_3, with some high field strength elements (HFSE), Th and U, but very low values of most other elements. The remaining granites are: two samples with ~69.5 wt. % SiO_2 and ~3.8 wt. % K_2O, four samples with ~72 wt. % SiO_2 and ~3.1 wt. % K_2O (Fig. 7b). The granites are weakly peraluminous, with aluminum saturation index (ASI) of 1.0–1.12 (Fig. 7c). The granodiorite has ASI=1.5. Their A/NK (molar $Al_2O_3/[Na_2O+K_2O]$) ratios range from 1.79 to 2.78 with an average of 2.10 (Fig. 7c). All granites plot well within the subalkaline field of Maniar & Piccoli (1989) (Fig. 7d).

Harker variation diagrams of major and trace elements vs. SiO_2 allow the degree of mobility of elements to be assessed (not shown here). The MgO, Ga, Eu and Nd show systematic decreasing abundance with increasing SiO_2. The K_2O, Na_2O, and other large-ion lithophile elements such as Rb and Ba, together with S, show a scattered distribution with no recognizable trend. Others like Al_2O_3, P_2O_5, TiO_2, La and Y show a general decreasing trend with increasing SiO_2, but with considerable scatter. This scatter is greater than in many Cenozoic granites, suggesting some mobilization due to hydrothermal alteration or metamorphic processes, or mixing of more than one magma type (Pin & Paquette 1997; Bonnetti et al. 2018). Decreasing Fe_2O_3, MgO, CaO, TiO_2, Ba, Eu, and Sr with increasing SiO_2 contents are consistent with fractional crystallization and can be related to fractionation of plagioclase, clinopyroxene, hornblende, and apatite (Esna-Ashari et al. 2011). In a K_2O/Al_2O_3 versus Na_2O/Al_2O_3 diagram (not shown), all samples fall in the igneous (I-type) field, with Na_2O/Al_2O_3 in

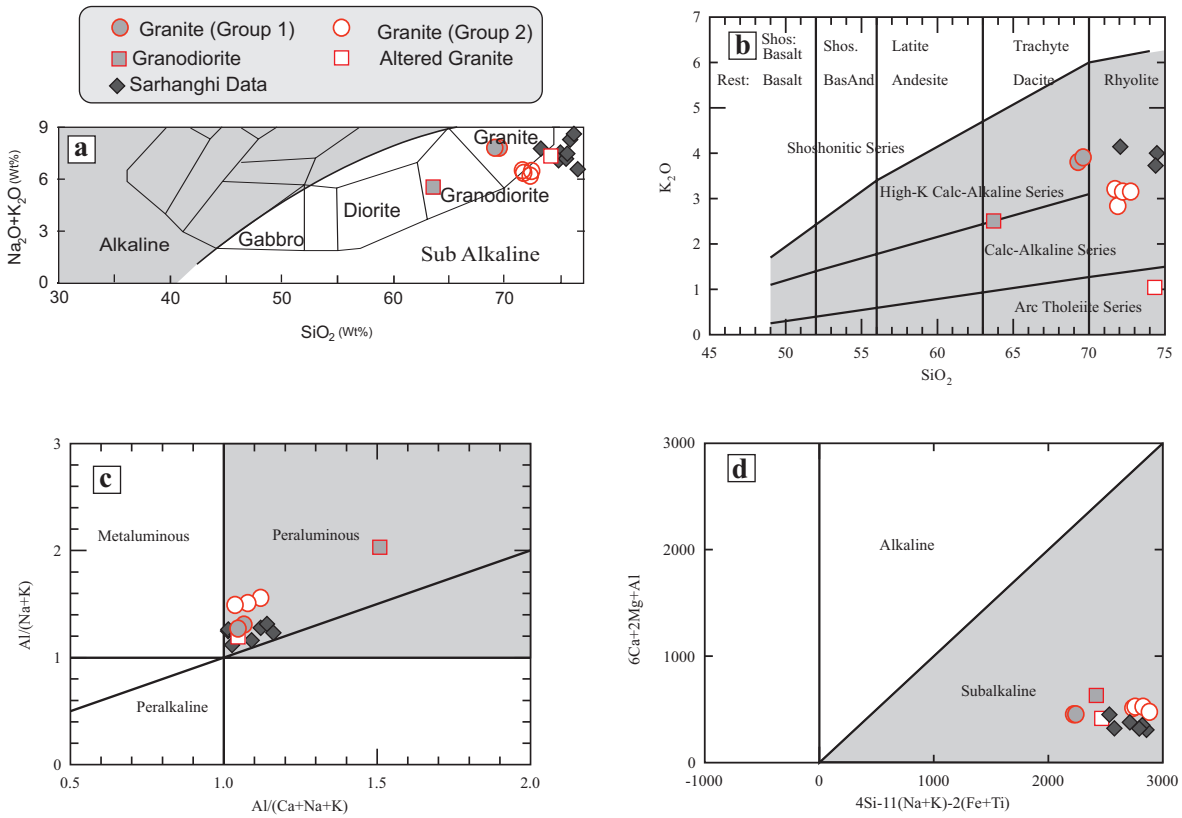

Fig. 7. Chemical classification of granitoid samples. **a** — Binary diagram of Na_2O+K_2O versus SiO_2 after Middlemost (1986), showing most of the samples located in the rhyolite (granite) field and one in the dacite (granodiorite) field. **b** — Binary diagram of K_2O versus SiO_2 (Maniar & Piccoli 1989), the analyzed samples range from calc-alkaline to high K calc-alkaline series (the arc tholeiite sample is altered). **c** — Binary diagram of A/(CNK) vs. A(NK)[molar $Al_2O_3/CaO+Na_2O+K_2O$ versus Al_2O_3/Na_2O+K_2O] (Maniar & Piccoli 1989) showing the peraluminous composition of the garnet granites. **d** — Binary diagram of 6Ca+2Mg+Al versus 4Si−11(Na+K)−2(Fe+Ti) (Maniar & Piccoli 1989). All granitoid samples fall in the sub alkaline field.

the range of 0.24 to 0.26. There is a systematic inverse correlation between P_2O_5 and SiO_2 (not shown), also an indication of I-type origin (Chappell & White 1992).

In Zeber-Kuh, the concentration of P_2O_5 ranges between 0.18 to 0.02 wt. %. Apatite-rich rocks are peraluminous with P_2O_5 contents ranging from 0.05 to 3.4 wt. % (Szopa et al. 2013). F, Mn, Sr and rare earth elements (REE) in apatite vary systematically with the composition of the host magma and thus have high potential as petrogenetic tracers (Belousova et al. 2002). More specifically, the F and Mn contents of apatite can be used as an indicator of magma aluminosity or differentiation index (Miles et al. 2014). Apatite and biotite in the Western Tatra Mts. (S-Poland, Western Carpathians) represent an early cumulate (Szopa et al. 2013; Miles et al. 2014). Feldspar and textural relations may reflect the interaction of the crystal faces of both minerals and support a model based on local saturation of P, Ca, and F versus K, Na, Al, Si, and Ba in the border zones (Szopa et al. 2013). The presence of apatite-rich rocks may be linked to the continuous mixing of felsic and mafic magmas, creating unique phosphorus- and aluminum-rich magma portions (Szopa et al. 2013; Miles et al. 2014). Although the Zeber-Kuh garnet granite is highly felsic rock with 69–74.5 wt. % SiO_2, scatter of some element in Harker type diagram indicate the mixing or contamination of magma during crystallization. The close relationship of apatite and feldspar in Zeber-Kuh could indicate that the slow diffusion in the phosphorus-rich magma pockets favored the local saturation and simultaneous crystallization of apatite and feldspars in a crystal-laden melt (Belousova et al. 2002; Szopa et al. 2013).

The Zr/Y ratio for the studied rocks is >4.5 indicating calc-alkaline affinity in a plot of Zr vs. Y (Fig. 8). In a binary plot of Zr vs. $10^4 \times Ga/Al$ (Fig. 9a), all samples lie in the field of S and I type granite. The ternary diagram of Rb–Ba–Sr (Fig. 9b) of El Bouseily & El Sokkary (1975) for granitic rocks, indicates for these rocks a granitic trend typical of differentiated granites with Ba enrichment and low Rb and Sr. According to this diagram, the granodiorite plots on the boundary of the granite with the granodiorite–quartz diorite field (differentiated trend) and some samples plot in the anomalous granite field. A few samples lie in the normal granite field because of the high Ba concentrations, which are typically associated with high temperature K-feldspars in normal granites.

In the tectonic discrimination diagram of Th/Yb vs. Nb/Yb or Ta/Yb, the granites fall in the continental arc field (Fig. 10),

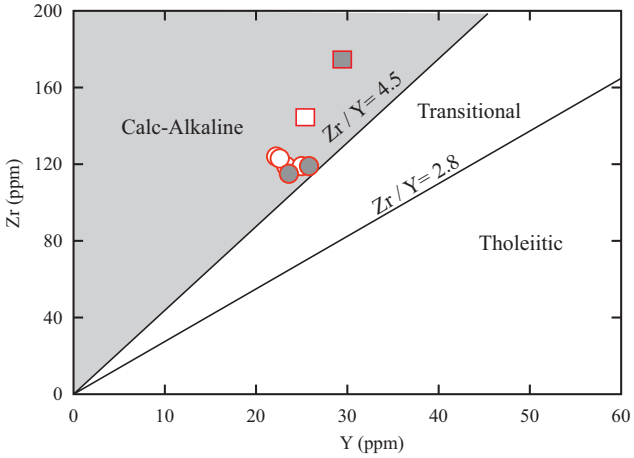

Fig. 8. Binary diagram of Zr vs Y (Ross & Bédard 2009) used to differentiate between different magma types. All the studied samples lie in the calc-alkaline field.

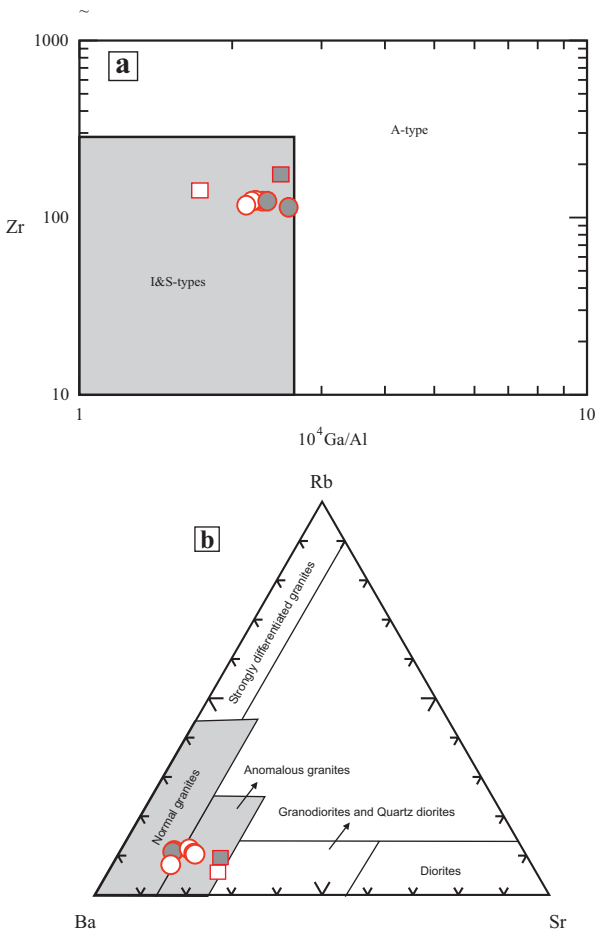

Fig. 9. Discrimination of I- and S-types of granite. **a** — Binary diagram of Zr vs 10^4Ga/Al (Whalen et al. 1987); all samples lie in the I- and S-type granite field. **b** — Rb–Ba–Sr ternary diagram (El Bouseily & El Sokkary 1975) for granitic rocks. It indicates a granitic trend typical of differentiated granites with Ba enrichment and low Rb and Sr. According to this diagram, the Zeber-Kuh garnet granite and granodiorite samples plot in the quartz diorite (differentiated trend) and anomalous granite fields, with a close association of Ba and Sr.

indicating the effect of Th enriched subduction fluids or crustal contamination. On various plots involving Rb, Y, Nb, and/or Ta, all of the samples classify as within-plate granite or volcanic arc granite (Fig. 11). A plot of Nb vs Yb (not shown) after Pearce et al. (1984) used by Mollai et al. (2019) for the tectonic setting of the Tapeh Tagh Granite Gneisses and other Cadomian rocks of east Central Iran also shows that all Zeber-Kuh samples fall in the within plate granite and VAG fields. One of the most characteristic features of magma was generated in the supra-subduction zone is the enrichment of LILE (Rb, K, Th, U, Sr and Pb) as well as depletion of the high field strength elements like Nb and Ti as well as the HREE like Yb (Castillo & Newhall 2004). The REE patterns show mild LREE fractionation, a small Eu anomaly and an almost flat pattern of HREE (Fig. 12a). Plots of trace elements relative to primitive mantle for the unaltered granites (Fig. 12b) show that Cs and Rb are enriched more than Ba and Th, and that Nb, Ta, P and Ti are relatively depleted and $(La/Yb)_N$=11.3. The consistency of both the REE and the HFSE suggests that neither has been influenced by alteration, nor were such elements concentrated in small amounts of late accessory minerals. Thus, they can be used to interpret the petrogenesis of the granites.

The REE patterns in zircons (Fig. 12c) show progressive enrichment from LREE to HREE with a positive Ce anomaly and a negative Eu anomaly. The range of concentrations of the REE is characteristic of magmatic zircons from felsic magmas (Hoskin & Ireland 2000; Hoskin & Schaltegger 2003). These anomalies may indicate oxidizing conditions, as proposed from the *P–T* pseudosections (Fig. 6), although they are also influenced by plagioclase fractionation (Smythe & Brenan 2015; Loader et al. 2017).

U–Pb geochronology

A feature of many of U–Pb geochronology studies is an implicit assumption that all zircons present in the host igneous rock are crystallized from the surrounding melt (Samperton et al. 2015). However, it has long been recognized that zircons present in an igneous rock can be inherited either from the surrounding country rock or source region (xenocrysts) (Samperton et al. 2015), or from earlier phases of magmatism or the magmatic plumbing system (antecrysts). Distinguishing these different origins for zircon crystals or domains within crystals is not straightforward (Pankhurst & Pidgeon 1976; Schaltegger et al. 2015). The typology study of zircon populations from granitic rocks led to the proposition of a genetic classification with three main divisions: (1) granites of crustal or mainly crustal origin; (2) granites of crustal + mantle origin, hybrid granites; (3) granites of mantle or mainly mantle origin (Pupin 1980).

Zircon grains were separated from three samples (HP3, HP4 and KS17) of coarse-grained garnet granite. From these three samples, 42 zircon grains were analyzed. The U–Pb age together with trace element abundances for zircon are listed in

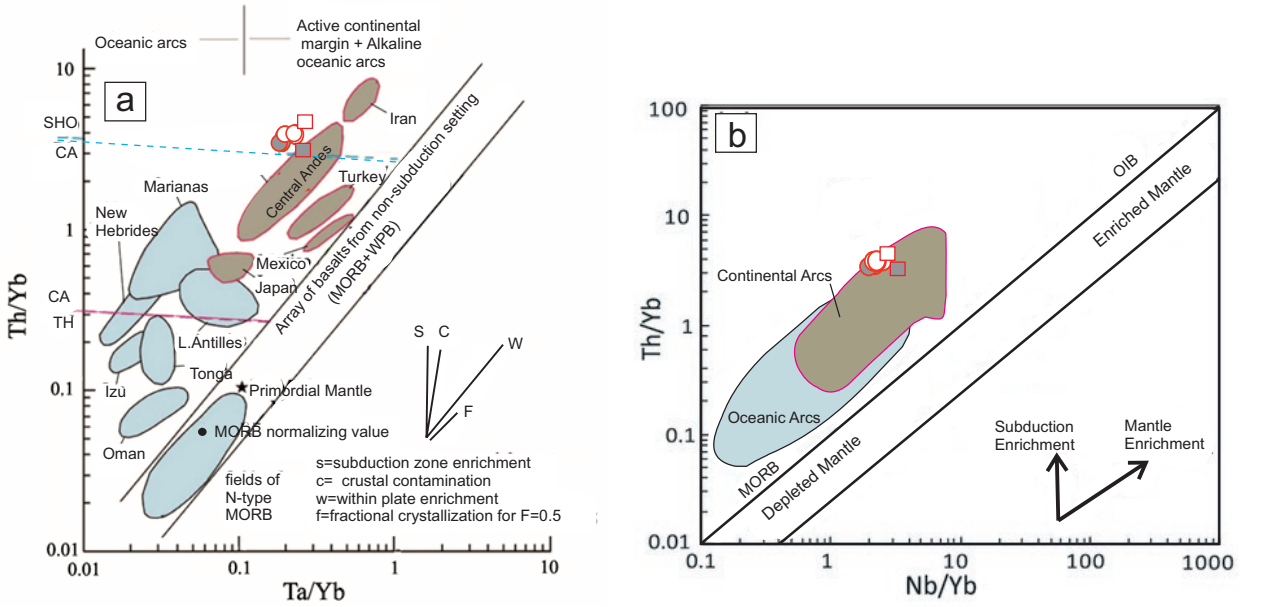

Fig. 10. a — Plot of Th/Yb versus Ta/Yb (Bowden & Kinnaird 1984). **b** — Plot of Th/Yb versus Nb/Yb (after Pearce 2008). All of the samples fall into the high Th/Yb field near active continental arc environments on the binary diagram, indicating the influence of Th enriched subduction fluids or crustal interaction and contamination. Vectors indicate the influence of subduction component (S), within-plate enrichment (W), crustal contamination (C), and fractional crystallization (F). Dashed lines separate boundaries of the tholeiitic (TH), calc-alkaline (CA), and shoshonitic (SHO) fields. Values of N-MORB, E-MORB, OIB, and WPB are from Sun & McDonough (1989). Also plotted are Emeishan high-Ti (HT) and low-Ti (LT1 and LT2) basalts, data from Xu et al. (2001); Xiao et al. (2004); Zhang et al. (2006).

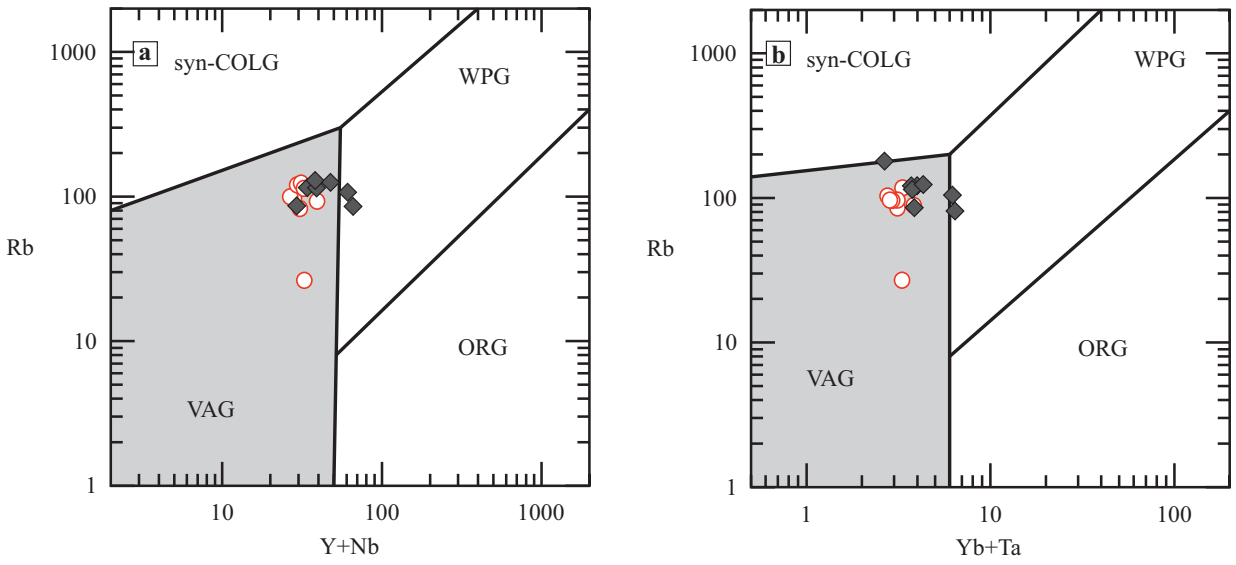

Fig. 11. Tectonic setting discrimination diagrams (Pearce et al. 1984): **a** — Rb vs (Y+Nb); **b** — Rb vs (Y+Ta). All samples fall in the VAG field. Abbreviations: WPG=Within Plate Granite, ORG=Ocean Ridge Granite, VAG=Volcanic Arc Granite, Syn-COLG=Syn-Collisional Granite.

Electronic Supplement S1. Cathodoluminescence images of zircon grains from the studied samples show strong luminescence and well-developing zoning with oscillatory bands, which is typical for magmatic zircons. Cathodoluminescence and LA-ICP-MS or ion microprobe analysis are used to provide increased confidence for the discrimination of inherited zircons from autocrystic zircons and determination of the emplacement age (Schaltegger et al. 2015).

Zircon grains from sample HP3 of grey garnet granite (Fig. 13) were mainly euhedral to subhedral. Some of the grains appeared broken, stubby, and elongated or equant prismatic in shape with oscillatory zoning. Their size ranged between 50 and 200 μm. Fourteen zircons were analyzed, with nine within 10 % of concordance forming a cluster with a Concordia age of 534.4±6.0 Ma (n=9, MSWD=1.8) and a TuffZirc age of 532.6±7.5 Ma (Fig. 13).

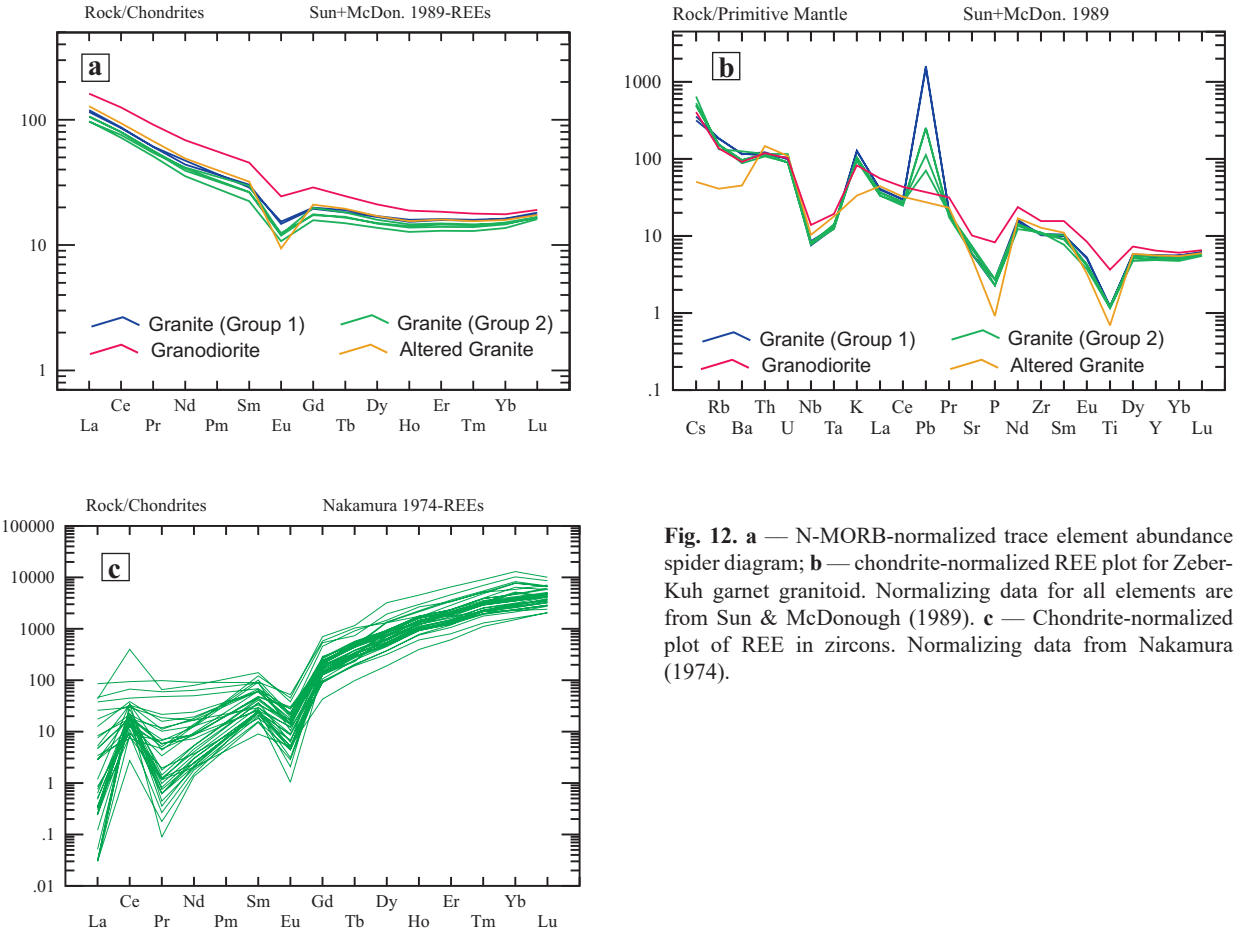

Fig. 12. a — N-MORB-normalized trace element abundance spider diagram; **b** — chondrite-normalized REE plot for Zeber-Kuh garnet granitoid. Normalizing data for all elements are from Sun & McDonough (1989). **c** — Chondrite-normalized plot of REE in zircons. Normalizing data from Nakamura (1974).

Compatible trace-elements like U, Th, and the REE reflect differentiation of these elements in the host melt (Hoskin & Schaltegger 2003) The HP3 zircon grains have high Th/U ratios ranges between 0.95 and 0.36 with an average of 0.63. The REE patterns (Fig. 12c) show progressive enrichment from LREE to HREE with a positive Ce anomaly and a negative Eu anomaly. The range of concentrations of the REE is characteristic of magmatic zircons from felsic magmas (Hoskin & Schaltegger 2003).

Fifteen points from zircon grains of sample HP4 were analyzed. Zircons are generally prismatic with lengths of 100–200 μm and length/width ratios of 2:1 to 3:1, and show oscillatory zoning with wide metamorphic growth rims. Comparatively, the size of grains of this sample is smaller than in other samples. Nine analyzed points form a linear discordia line, but only two are 90 % concordant or better. These nine points give a Concordia age of 533.1±3.4 Ma (n=9, MSWD=0.63) and a TuffZirc age of 531.9±7.0 Ma (Fig. 12). Trace elements including REE are similar to HP3, with Th/U ratios ranges from 0.79 to 0.34 with average of 0.61 and confirm that there is oscillatory zoning. Euhedral zircon grains from gneiss sample HP-4 exhibited uniform to oscillatory-zoned internal structures and high Th/U ratios (0.79 to 0.57) typical of magmatic minerals. Zircon grains from this sample experienced variable later overprint with the growth of different rims resulting in these nine points give a Concordia age of 533.1±3.4 Ma (n=9, MSWD=0.63) and a TuffZirc age of 531.9±7.0 Ma. This is, therefore, considered to be the emplacement age of sample HP-4. The upper intercepts are of high errors, which means the nearly complete resetting of the U–Pb system in zircon or regrowth of the zircon crystal during the Cambrian. The upper intercept is calculated at 3438±390 Ma (MSWD=2.8).

Thirteen points from zircons in sample KS17, pink foliated garnet granite, were analyzed. The zircon grains are euhedral in shape. The oscillatory zoned cores show characteristics indicative of magmatic origin, whereas the structure of less common overgrowth rims and some single grains show characteristics typical of metamorphic origin, indicating that these zircons underwent significant alteration by late metamorphic or thermal events (Grant et al. 2009). Th/U ratios range from 1.55–0.21 with average of 0.66. Eight zircons yielded a spread of characteristically Cadomian ages (Fig. 12). These eight analyses are at least 97 % concordant and give a Concordia age of 553±17 Ma (n=8, MSWD=9.1). A coherent group of four of these points gave TuffZirc age of 573.3±2.4 Ma. One of the other point gave a young age of ca. 200 Ma, suggesting some Cimmerian resetting. Two zircons have 0.75 Ga ages and two others 2.5 Ga ages, all apparently reflecting inheritance from older crust.

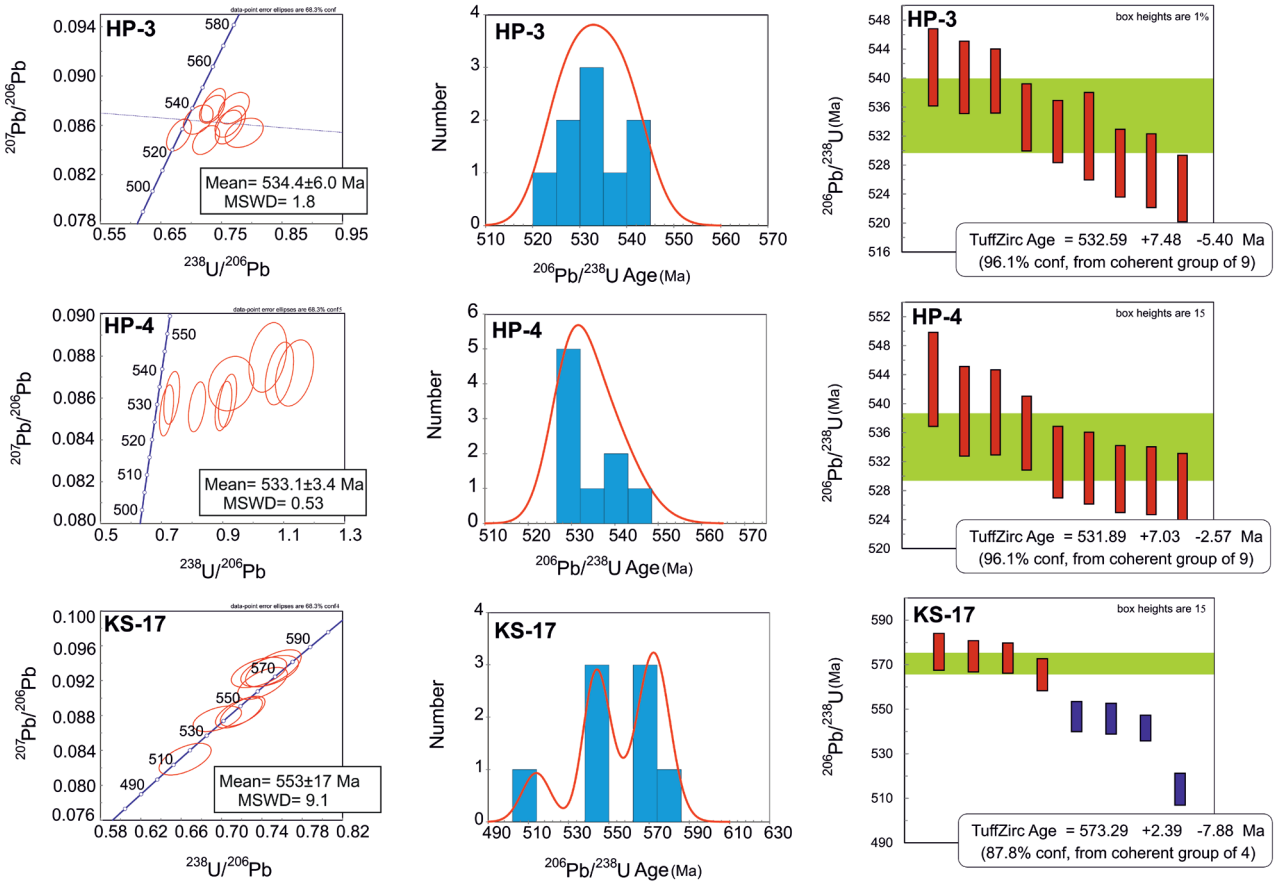

Fig. 13. Results of zircon U–Pb geochronology of samples HP3, HP4 and KS17 of garnet granitoids from Zeber-Kuh. Sample HP3: Fourteen zircons were analyzed, with nine within 10 % of concordance forming a cluster with a Concordia age of 534.4±6.0 Ma (n=9, MSWD=1.8) and a TuffZirc age of 532.6±7.5 Ma. Sample HP4: Fifteen points were analyzed, Nine analyzed points form a linear discordia line, but only two are 90 % concordant or better. These nine points give a Concordia age of 533.1±3.4 Ma (n=9, MSWD=0.63) and a TuffZirc age of 531.9±7.0 Ma. Sample KS17: Thirteen points were analyzed. Eight zircons with characteristically Cadomian ages are at least 97 % concordant and give a Concordia age of 553±17 Ma (n=8, MSWD=9.1). A coherent group of four of these points gave Tuff Zirc age of 573.3±2.4 Ma.

Discussion

Interpretation of zircon geochronology

Most of the analyzed zircon grains showed typical oscillatory zoning and have Th/U ratios higher than 0.1, suggesting the zircons were of igneous origin. Metamorphic zircon either lacks zonging or shows weak, cloudy, planar or patchy zoning (Pupin 1980; Mollai et al. 2019; Méheut et al. 2021). The zoning reflects the compositional variation of Zr and Si and more important variations in Hf, P, Y, the REE, U, and Th, up to an order of magnitude for some of these elements (Claiborne et al. 2010). Zircons in the Zeber-Kuh are characterized by margins as well as cores with luminescence and zoning with oscillatory bands, which is typical for magmatic zircons. With increasing differentiation of the host melt, zircon tends to have higher compatible trace-element levels like U, Th, and REE (Belousova et al. 2002). Topology and CL and BSE images of zircon from the Zeber-Kuh garnet granite can be compared with zircon grains of the Menderes Massif in western Turkey. The two samples of grey granite from Zeber-Kuh show similar Pb loss and Concordia ages of 534 Ma (Fig. 12), and the third gave a cluster of zircons with an age of 573 Ma. Dating of zircons from other Cadomian plutons in the general region has yielded Concordia ages between 576±3 and 536±5 for magmatic zircons (Rossetti et al. 2015). Zircon grains from sample HP-3 (Fig. 13) were euhedral, but some grains were broken into fragments. A light overgrowth rim is easily observed on the oscillatory core. A total of fifteen analyses clustered around the concordant curve and defined a concordant line with a lower intercept at 534 Ma (n=15, MSWD=0.96). This is, therefore, considered to be the emplacement age of sample HP-3.

The foliated pink granite KS17 shows a spread of ages along Concordia (Fig. 13). Given the two 0.75 Ga and two 2.5 Ga analyses from magmatically zoned zircon cores (Electronic Supplement S1), there appears to be incorporation of older crustal material with igneous zircons. The one grain that gave an age of 200±3 Ma probably reflects metamorphic outgrowth, as inferred from CL images, during Triassic accretion

to Eurasia in the Cimmerian orogeny. Ablation of minor amounts of inherited zircon during analysis could account for the spread of analyses along Concordia. The ages of the four pre-Cadomian zircons correspond to the two most prominent pre-Cadomian peaks in detrital zircons from lower Paleozoic sandstones in Iran (Moghadam et al. 2016) and specifically in the lower Cambrian Zaigun sandstone (Honarmand et al. 2018), at 0.75 Ga and 2.5 Ga. The abundance of such old zircons in sample KS17 suggests that all such old detrital zircons could have been recycled through younger plutons.

Petrogenesis and magmatic source of upper Neoproterozoic garnet granite

The geochemical features indicate that the rocks are highly fractionated I-type granite and have undergone extensive fractional crystallization of hornblende, biotite and feldspar. Results are consistent with melting of an evolved lower crust source during the subduction of the Proto-Tethys Ocean. The emplacement of the Zarin granite is contemporaneous with the extension of a Cadomian continental arc on the north side of Gondwana, that rifted away to create the Rheic Ocean to its south (Nouri et al. 2018; Asadi Sarshar et al. 2020). Cadomian basement rocks in Iran are interpreted as an important link between western and eastern sectors of the upper Proterozoic–lower Paleozoic orogenic belts along the northern side of Gondwana, and the histories of the Rheic, Iapetus and Proto-Tethyan oceans (Moghadam et al. 2020).

Upper Neoproterozoic–Cambrian, orogenic, granitic gneisses such as the Zeber-Kuh exhibit geochemical characteristics typical of high silica content. This igneous body has an average composition of 71 wt. % SiO_2, 14 wt. % Al_2O_3, 3.8 wt. % Na_2O, 2.9 wt. % K_2O, 0.9 wt. % MgO, 0.3 wt. % TiO_2, and 0.1 wt. % P_2O_5. The ratio of Ga/Al is high, as is the ratio of iron to magnesium with lower levels of Ca, Mg, Ti, P, and Sr. Based on the Na_2O+K_2O versus SiO_2 diagram, the Zeber-Kuh was predominantly granite; only two samples plotted in the granodiorite field (Fig. 7b). The rocks are sub alkaline and peraluminous (Fig. 7c). The Zeber-Kuh granite was more enriched in LREE relative to HREE. La_N/Yb_N is high (average 11.3), Eu/Eu*<1 ranges between 0.22 to 0.12 with average 0.18 and Ce/Ce* ranges between 4.25 to 0.32 with an average of 3.4.

Contemporaneous positive Ce anomalies and negative Eu anomalies are a common observation in zircons (Fig. 12c). They seem to support oxidation of magma which is probable due to the presence of epidote. This has posed somewhat of a paradox, as Ce^{4+}, interpreted to represent oxidizing conditions, and Eu^{2+}, which is stable under reducing conditions, were thought to not coexist (Lauer & Morris 1977; Hoskin & Schaltegger 2003). This leads to the conclusion that other mechanisms, such as the fractionation of plagioclase, prior to or during zircon crystallization, are required to form simultaneous Ce and Eu anomalies. Using models for Ce redox state and for Eu, it is possible to estimate the coexisting Ce and Eu anomalies in zircon at equilibrium (Lauer & Morris 1977; Hoskin & Schaltegger 2003). This shows that the high affinity of zircon for Ce^{4+}, coupled with the stabilization of trace amounts of Ce^{4+} at relatively reducing conditions, can also account for this observation. Ce and Eu anomalies in zircon are also affected by the co-crystallisation of REE bearing phases, such as titanite. Based on the trace element chemistry of zircons from titanite-bearing intrusions associated with mineralisation of Cu–Au deposit neither zircon Eu/Eu*, nor Ce^{4+}/Ce^{3+} are robust proxies for melt redox conditions, because they are both too strongly dependent on melt REE concentrations, which are usually poorly constrained and controlled by the crystallization of titanite and other REE-bearing phases. Ce and Eu are unique among the other REE, which are usually trivalent, whereas Ce and Eu may also exist as Ce^{4+} and Eu^{4+}.

These data are consistent with melting in the stability field of plagioclase with little contribution to the melt from refractory minerals such as zircon, and apatite. The REE and trace element patterns, which display negative Eu and Sr anomalies on the spider diagrams (Fig. 12a and b), indicate that the crystal-liquid equilibrium involved feldspar either in the source or in a melt. The negative anomalies of Eu, Ba, and Sr were interpreted as differentiation of plagioclases in a stable mineral phase during partial melting of the source rock (Hanson 1978; Moghadam et al. 2020). Minerals such as garnet have influenced Y abundance, while biotite could have controlled Nb enrichment. Orthogneiss in the area (Mollai et al. 2019) with high modal biotite also displays enriched Nb content. Important evidence for the origin of the garnet granite is their REE patterns. The observed, almost flat, or slightly decreasing HREE patterns indicate no residual or fractionating garnet, and the slight rise from Dy to Lu suggests amphibole fractionation (Fig. 12b). The presence of slight to significant negative Eu anomalies, which played an important role in the petrogenesis, could be due to the fractionation of feldspar and/or residual feldspar (Pearce et al. 1984; Furman et al. 1992; Pearce 2008). The rock consistently plots in the geochemical field of Active Continental Margins. Based on the whole-rock geochemistry and REEs, the garnet granite is thought to have crystallized from the subduction-related partial melt of the volcanic arc granite (VAG; Fig. 11). The same data in Fig. 10 plot in the continental arc field. It is further suggested that east-central Iran was in a similar tectonic setting to the Tauride belt in western central Turkey, and to Gondwana terrains in North Africa and southern Europe during the Cadomian (Alavi 1994; Ramezani & Tucker 2003; Bozkaya et al. 2006; Gürsu & Göncüoglu 2006).

Geodynamic implications

The Gondwana supercontinent formed during the late Neoproterozoic and remained stable over at least 300 Ma from Cambrian to Triassic. The supercontinent was an amalgamation of east and west Gondwana in the Pan-African orogeny (Stern 2008; Mollai et al. 2019). The back-arc basin setting of the lower Cambrian meta-magmatic rocks of Turkey is in agreement with the geodynamic model for Anatolia, which

suggests that the late Neoproterozoic–early Cambrian volcanism in southern Turkey was related to the southward subduction at the northern margin of Gondwana. Magmatic 530–630 Ma rocks from the Cadomian magmatic arc have been reported from central, north-west, north-east and eastern Iran (Table 1), as well as Azerbaijan, and are related to the Pan-African tectonic-magmatic episode (Ramezani & Tucker 2003; Azizi & Moinevaziri 2009). U–Pb zircon and whole-rock Rb/Sr dating of basement rocks in Iran is consistent with the rocks being from the late Ediacaran–early Cambrian and of Cadomian magmatic arc emplacement age (Haghipour 1974; Moghadam et al. 2016). The Cadomian magmatism in Iran began with the interaction of the arc-related magma with the Gondwana basement above the southward-subducting, northern margin of Gondwana at ca 570–600 Ma (Fig. 14). Subsequently, at ca. 560–590 Ma, a back-arc basin was initiated behind the Cadomian magmatic arc. The oldest phase of Zeber-Kuh magmatism, represented by the 573 Ma date from the foliated pink granite (KS17), dates from this time. Anatexis is inferred from the inherited old zircons in this granite.

The trace and REE characteristics of Zeber-Kuh garnet granite are similar to arc-related granites and show comparable compositions to other Cadomian intrusions in East-Central and Central Iran (Rossetti et al. 2015; Moghadam et al. 2016; Mollai et al. 2019). The petrography shows some development of secondary minerals, and some zircon outgrowths developed during the Cimmerian orogeny, so that care must be taken in interpreting more mobile elements, as shown by the trace element composition of altered granite Zb22 (Table 1). The stable REE, Th, Nb and Ta values indicate formation in a continental arc environment (Fig. 10). The whole-rock geochemistry suggests that the Zeber-Kuh granite is an I-type granite. The Na_2O/Al_2O_3 ratio and the inverse correlation between P_2O_5 and SiO_2 are characteristic of I-type origin (Chappell & White 1992). The zircons are characteristically of igneous origin and most have an age similar to the inferred Cadomian emplacement age. Most of the analyzed zircon grains showed typical oscillatory zoning and have Th/U ratios higher than 0.1, suggesting the zircons were of igneous origin. Nevertheless, there are some features that might indicate an S-type origin for the Zeber-Kuh granite, or a component of the granite. The whole-rock geochemistry is mildly peraluminous (Fig. 7c), particularly for the one granodiorite sample. However, peraluminous, silica-rich (SiO_2 >71 wt. %) I-type granites are relatively common world-wide. Magmatic garnet is most commonly a component of S-type granites (Sheibi et al. 2010), but is also found in some I-type and A-type granites (Du Bray 1988). One sample of the Zeber-Kuh granite has 33 % recycled older igneous zircons, suggesting S-type affinity. Because all the rock types in the Zeber-Kuh complex have faulted contacts, the surrounding lower amphibolite facies (epidote-amphibolite) metamorphic rocks and the granitic gneisses have an unknown relationship to the garnet granite and thus provide limited evidence of the conditions under which the granite was emplaced.

Most granite plutons have been constructed by multiple batches of magma. This is easily recognized when emplacement has taken place over an extended period, or when different batches have contrasting whole-rock geochemistry. Where magma batches have been well mixed, detailed study of mineral components may be necessary to distinguish multiple sources (Gao et al. 2016; Rong et al. 2018). Thus many granites in the world are neither 100 % I-type nor 100 % S-type. One of the most characteristic features of the Zeber-Kuh granite is the presence of isotropic garnet. Anisotropic garnet with a low birefringence and zoning is usually the product of metasomatism (Hariya & Kimura 1978; Mollai et al. 2014, Mollai et al. 2019). Analyses of garnets in this region by Rossetti et al. (2015) show that they compositionally conform to an almandine–grossular solid solution ($Alm_{58–70}$, $Grs_{19–31}$) with only minor $Prp_{3–9}$ and $Sps_{0–13}$. There is rimward decrease in the spessartine component compensated by almandine enrichment. These garnets are most similar to some magmatic high-Alm garnets reported from the Neoproterozoic Galiléia batholith in Brazil (Narduzzi et al. 2017). The compilation of experimental data by Narduzzi et al. (2017) suggests that such low-pyrope garnets, in equilibrium with epidote and muscovite, are characteristic of magma crystallization at pressures greater than 0.8 GPa (~25 km depth) and at temperatures below 700 °C with >10 % water.

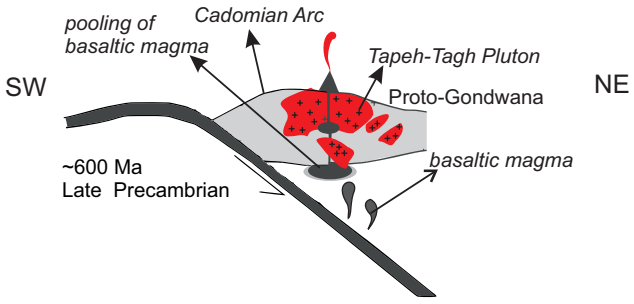

Fig. 14. Summary of the geodynamic tectonic setting of Cadomian crustal terranes within east-central Iran, with special reference to Zeber-Kuh garnet granitoids (see text for explanation). Modified after Stern (1994); Gürsu & Göncüoglu (2006); Linnemann et al. (2014); Moghadam et al. (2016); Honarmand et al. (2018).

Conclusions

The Zeber-Kuh garnet granite is weakly peraluminous and has I-type granite geochemical features. Like other granites in the northern Kashmar–Kerman tectonic zone, it is characterized by the presence of magmatic garnet showing alteration to biotite and secondary epidote. The compositional data and the physical conditions of crystallization reported for solid phases such as biotite or white mica are consistent with magmatic equilibration with garnet. Thus fractionation of Mn in garnet as well as the proportion of garnet that crystallizes is roughly controlled by the evolving composition of the different granitic facies. All available data, including field and petrographic relationships, mineral chemistry, bulk major and

trace element compositions, and isotopic ratios support differentiation by fractional crystallization of magma in the middle crust. Mineral assemblages are plagioclase and subordinate quartz, garnet, biotite K-feldespar ± muscovite. Remarkably, garnet crystallized throughout the differentiation sequence of the Zeber-Kuh garnet granite (SiO_2=65.70–74.57 wt. %). Its textural characteristics and chemical compositions indicate that it could have formed by direct nucleation and subsequent crystallization from the peraluminous magma in equilibrium with solid phases such as biotite and muscovite. Fractionation of Mn in garnet as well as the proportion of garnet that crystallizes is roughly controlled by the evolving composition of the different granitic facies. Contrarily, garnet housed in granitic rocks, rich in spessartine, must be considered in very felsic magmas (SiO_2=64–74 %) crystallizing above 680 °C. The primary minerals imply an origin at pressures greater than 6–8 kbar (~25 km depth) and at temperatures above 700 °C with >10 % water, thus likely in a fore-arc setting (Dahlquist et al. 2007). The stable REE, Th, Nb and Ta values also indicate formation in a continental arc environment.

The zircons are characteristically of igneous origin and most have an age similar to the inferred Cadomian emplacement age. The age of the main phase of the Zeber-Kuh granite, ~534 Ma, correspond to the youngest regionally dated Cadomian magmatism. Foliated pink granite is older (~573 Ma) and contain recycled older igneous zircons dating from 0.75 and 2.5 Ga, corresponding to widely recognized age peaks in Paleozoic detrital sediments. Most of the analyzed zircon grains have REE compositions, typical oscillatory zoning and Th/U ratios higher than 0.1, characteristic of an igneous origin, but some have metamorphic outgrowths that probably date from the Cimmerian orogeny. The trace and REE characteristics of Zeber-Kuh garnet granite are similar to arc-related granites and show comparable compositions to other Cadomian intrusions in East-Central and Central Iran. Magmatic rocks of 530–630 Ma from the Cadomian magmatic arc have been reported from central, north-west, north-east and eastern Iran (Table 1) as well as Azerbaijan, and are related to the Pan-African tectonic-magmatic episode. The Cadomian magmatism in Iran began with the interaction of the arc-related magma with the Gondwana basement above the southward-subducting, northern margin of Gondwana at ca 570–600 Ma, but plutons of the main igneous phase give mean ages of 527 Ma and are part of the of late Neoproterozoic–early Paleozoic magmatic activity in peri-Gondwana. Our geochemical and geochronological data are consistent with late Neoproterozoic–early Paleozoic arc magmatism along the active continental margin of north Gondwana. All the above blocks were part of Gondwana until later in the Paleozoic, when they separated during Neotethys rifting and were re-joined in the Oligo–Miocene period.

Acknowledgements: We gratefully acknowledge the financial support for this research made possible by the Vice Presidency of Research and Technology, Mashhad Branch, Islamic Azad University, Mashhad, Iran. I would like to offer special thanks to my friend Professor M. Pandit (Rajasthan, India), Dr. M. Jawanbakhat and our late friend A Pourlatifi. We would like thanks the Activation Laboratories, Canada for geochemical analysis and State Key Laboratory of Geological Processes and Mineral Resources (SKLGPM), China University of Geosciences, Wuhan, China for Cathodoluminescence which supported the LA-ICP-MS zircon analyses. And also thanks to Prof. Federico Rossetti for useful suggestions and permitting us to use his published data on the area. Special thanks to prof. David J.W. Piper from Natural Resources Canada for final linguistic correction and proofreading of the paper as well as prof. Georgia Pipper from Saint Mary's University of Canada for payment of color figures and extra pages. We are very grateful to Prof. Igor Petrík, Handling Editor in Bratislava, for useful suggestions, improving the Petrological section and calculating pseudosections of the Zeber-Kuh granite. Also, Silvia Antolíková, Ph.D., Managing Editor of Geologica Carpathica, for facilitating all of the communications.

References

Agard P., Omrani J., Jolivet L. & Mouthereau F. 2005: Convergence history across Zagros (Iran): constraints from collisional and earlier deformation. *International Journal of Earth Sciences* 94, 401–419. https://doi.org/10.1007/s00531-005-0481-4

Alavi M. 1994: Tectonics of the Zagros orogenic belt of Iran: new data and interpretations. *Tectonophysics* 229, 211–238. https://doi.org/10.1016/0040-1951(94)90030-2

Andersen T. 2002: Correction of common lead in U-Pb analyses that do not report ^{204}Pb. *Chemical Geology* 192, 59–79. https://doi.org/10.1016/S0009-2541(02)00195-X

Asadi Sarshar M., Moghadam H.S., Griffin W.L., Santos J.F., Stern R.J., Ottley C.J., Sarkarinejad K., Sepidbar F. & O'Reilly S.Y. 2020: Geochronology and geochemistry of exotic blocks of Cadomian crust from the salt diapirs of SE Zagros: the Chah-Banu example. *International Geology Review*, 1–22. https://doi.org/10.1080/00206814.2020.1787236

Azizi H. & Moinevaziri H. 2009: Review of the tectonic setting of Cretaceous to Quaternary volcanism in northwestern Iran. *Journal of Geodynamics* 47, 167–179. https://doi.org/10.1016/j.jog.2008.12.002

Belousova E., Griffin W.L., O'Reilly S.Y. & Fisher N. 2002: Igneous zircon: trace element composition as an indicator of source rock type. *Contributions to Mineralogy and Petrology* 143, 602–622. https://doi.org/10.1007/s00410-002-0364-7

Boehnke P., Watson E.B., Trail D., Harrison T.M. & Schmitt A.K. 2013: Zircon saturation re-revisited. *Chemical Geology* 351, 324–334. https://doi.org/10.1016/j.chemgeo.2013.05.028

Bonnetti C., Liu X., Mercadier J., Cuney M., Deloule E., Villeneuve J. & Liu W. 2018: The genesis of granite-related hydrothermal uranium deposits in the Xiazhuang and Zhuguang ore fields, North Guangdong Province, SE China: Insights from mineralogical, trace elements and U-Pb isotopes signatures of the U mineralisation. *Ore Geology Reviews* 92, 588–612. https://doi.org/10.1016/j.oregeorev.2017.12.010

Bowden P. & Kinnaird J. 1984: The petrology and geochemistry of alkaline granites from Nigeria. *Physics of the Earth and Planetary Interiors* 35, 199–211. https://doi.org/10.1016/0031-9201(84)90043-8

Bozkaya Ö., Gürsu S. & Göncüoglu M.C. 2006: Textural and mineralogical evidence for a Cadomian tectonothermal event in the

eastern Mediterranean (Sandıklı-Afyon area, western Taurides, Turkey). *Gondwana Research* 10, 301–315. https://doi.org/10.1016/j.gr.2006.04.009

Castillo P. & Newhall C. 2004: Geochemical constraints on possible subduction components in lavas of Mayon and Taal volcanoes, southern Luzon, Philippines. *Journal of Petrology* 45, 1089–1108. https://doi.org/10.1093/petrology/egh005

Chappell B.W. & White A. 1992: I-and S-type granites in the Lachlan Fold Belt. *Earth and Environmental Science Transactions of the Royal Society of Edinburgh* 83, 1–26. https://doi.org/10.1017/S0263593300007720

Claiborne L.L., Miller C.F. & Wooden J.L. 2010: Trace element composition of igneous zircon: a thermal and compositional record of the accumulation and evolution of a large silicic batholith, Spirit Mountain, Nevada. *Contributions to Mineralogy and Petrology* 160, 511–531. https://doi.org/10.1007/s00410-010-0491-5

Connolly J.A.D. 1990: Multivariable phase diagrams; an algorithm based on generalized thermodynamics. *American Journal of Science* 290, 666–718. https://doi.org/10.2475/ajs.290.6.666

Connolly J.A.D. 2005: Computation of phase equilibria by linear programming: a tool for geodynamic modeling and its application to subduction zone decarbonation. *Earth and Planetary Science Letters* 236, 524–541. https://doi.org/10.1016/j.epsl.2005.04.033

Dabiri R., Akbari-Mogaddam M. & Ghaffari M. 2018: Geochemical evolution and petrogenesis of the eocene Kashmar granitoid rocks, NE Iran: implications for fractional crystallization and crustal contamination processes. *Iranian Journal of Earth Sciences* 10, 68–77.

Du Bray E.A. 1988: Garnet compositions and their use as indicators of peraluminous granitoid petrogenesis—southeastern Arabian Shield. *Contributions to Mineralogy and Petrology* 100, 205–212. https://doi.org/10.1007/BF00373586

Duchmand-Zadeh A. 1969: Métamorphisme et granitisation du Massif Chapedony-Iran Central. *Ph.D. dissertation, Faculté des Sciences*, Grenoble.

El Bahariya G.A. 2021: An Overview on the Classification and Tectonic Setting of Neoproterozoic Granites of the Nubian Shield, Eastern Desert, Egypt. In: René M., Aiello G., El Bahariya G. (Eds.): Geochemistry, Ch. 2. https://doi.org/10.5772/intechopen.95904

El Bouseily A. & El Sokkary A. 1975: The relation between Rb, Ba and Sr in granitic rocks. *Chemical Geology* 16, 207–219. https://doi.org/10.1016/0009-2541(75)90029-7

Esna-Ashari A., Hassanzadeh J. & Valizadeh M.-V. 2011: Geochemistry of microgranular enclaves in Aligoodarz Jurassic arc pluton, western Iran: implications for enclave generation by rapid crystallization of cogenetic granitoid magma. *Mineralogy and Petrology* 101, 195–216. https://doi.org/10.1007/s00710-011-0149-7

Etemad-Saeed N., Hosseini-Barzi M., Adabi M.H., Miller N.R., Sadeghi A., Houshmandzadeh A. & Stockli D.F. 2016: Evidence for ca. 560 Ma Ediacaran glaciation in the Kahar formation, central Alborz Mountains, northern Iran. *Gondwana Research* 31, 164–183. https://doi.org/10.1016/j.gr.2015.01.005

Furman T., Frey F.A. & Meyer P.S. 1992: Petrogenesis of evolved basalts and rhyolites at Austurhorn, southeastern Iceland: the role of fractional crystallization. *Journal of Petrology* 33, 1405–1445. https://doi.org/10.1093/petrology/33.6.1405

Gao P., Zheng Y.-F. & Zhao Z.-F. 2016: Distinction between S-type and peraluminous I-type granites: Zircon versus whole-rock geochemistry. *Lithos* 258, 77–91. https://doi.org/10.1016/j.lithos.2016.04.019

Ghorbani M. 2013: A summary of geology of Iran. In: The economic geology of Iran. *Springer*, 45–64.

Grant M.L., Wilde S.A., Wu F. & Yang J. 2009: The application of zircon cathodoluminescence imaging, Th–U–Pb chemistry and U–Pb ages in interpreting discrete magmatic and high-grade metamorphic events in the North China Craton at the Archean/Proterozoic boundary. *Chemical Geology* 261, 155–171. https://doi.org/10.1016/j.chemgeo.2008.11.002

Grebennikov A. 2014: A-type granites and related rocks: petrogenesis and classification. *Russian Geology and Geophysics* 55, 1353–1366. https://doi.org/10.1016/j.rgg.2014.10.011

Gürsu S. & Göncüoglu M.C. 2006: Petrogenesis and tectonic setting of Cadomian felsic igneous rocks, Sandıklı area of the western Taurides, Turkey. *International Journal of Earth Sciences* 95, 741–757. https://doi.org/10.1007/s00531-005-0064-4

Haghipour A. 1974: Petrology and tectonic activity of the pre-Cambrian sediments of Biabanak and Bafgh regions of Central Iran. *Geological Survey Iran, Rept* 34, 403.

Hanson G.N. 1978: The application of trace elements to the petrogenesis of igneous rocks of granitic composition, *Earth and Planetary Science Letters* 38, 26–43. https://doi.org/10.1016/0012-821X(78)90124-3

Hariya Y. & Kimura M. 1978: Optical anomaly garnet and its stability field at high pressures and temperatures. *Journal of the Faculty of Science, Hokkaido University* 18, 611–624.

Holland T. & Powell R. 2011: An improved and extended internally consistent thermodynamic dataset for phases of petrological interest, involving a new equation of state for solids. *Journal of Metamorphic Geology* 29, 333–383. https://doi.org/10.1111/j.1525-1314.2010.00923.x

Honarmand M., Xiao W., Nabatian G., Blades M.L., dos Santos M.C., Collins A.S. & Ao S. 2018: Zircon U–Pb–Hf isotopes, bulk-rock geochemistry and Sr–Nd–Pb isotopes from late Neoproterozoic basement in the Mahneshan area, NW Iran: Implications for Ediacaran active continental margin along the northern Gondwana and constraints on the late Oligocene crustal anatexis. *Gondwana Research* 57, 48–76. https://doi.org/10.1016/j.gr.2017.12.009

Horton B., Hassanzadeh J., Stockli D., Axen G., Gillis R., Guest B., Amini A., Fakhari M., Zamanzadeh S. & Grove M. 2008: Detrital zircon provenance of Neoproterozoic to Cenozoic deposits in Iran: Implications for chronostratigraphy and collisional tectonics. *Tectonophysics* 451, 97–122. https://doi.org/10.1016/j.tecto.2007.11.063

Hoskin P.W. & Ireland T.R. 2000: Rare earth element chemistry of zircon and its use as a provenance indicator. *Geology* 28, 627–630.

Hoskin P.W. & Schaltegger U. 2003: The composition of zircon and igneous and metamorphic petrogenesis. *Reviews in Mineralogy and Geochemistry* 53, 27–62. https://doi.org/10.2113/0530027

Jahangiri A. 2007: Post-collisional Miocene adakitic volcanism in NW Iran: geochemical and geodynamic implications. *Journal of Asian Earth Sciences* 30, 433–447. https://doi.org/10.1016/j.jseaes.2006.11.008

Jamshidibadr M., Tarabi S. & Qolizadeh K. 2020: Study of micro-textures and chemistry of feldspar minerals of East Sarbisheh volcanic complex (Eastern Iran), for evidence of magma chamber process. *Iranian Journal of Earth Sciences* 12, 10–31.

Javadi H.R., Ghassemi M.R., Shahpasandzadeh M., Guest B., Ashtiani M.E., Yassaghi A. & Kouhpeyma M. 2013: History of faulting on the Doruneh Fault System: implications for the kinematic changes of the Central Iranian Microplate. *Geological Magazine* 150, 651–672. https://doi.org/10.1017/S0016756812000751

Kumar H. & Pandit M. 2020: Recurrent seismicity in Rajasthan State in the tectonically stable NW Indian Craton. *Iranian Journal of Earth Sciences* 12, 1–9.

Lauer H. & Morris R.V. 1977: Redox equilibria of multivalent ions in silicate glasses. *Journal of the American Ceramic Society* 60, 443–451. https://doi.org/10.1111/j.1151-2916.1977.tb15530.x

Linnemann U., Gerdes A., Hofmann M. & Marko L. 2014: The Cadomian Orogen: Neoproterozoic to Early Cambrian crustal growth and orogenic zoning along the periphery of the West African Craton – Constraints from U–Pb zircon ages and Hf isotopes (Schwarzburg Antiform, Germany). *Precambrian Research* 244, 236–278. https://doi.org/10.1016/j.precamres.2013.08.007

Loader M.A., Wilkinson J.J. & Armstrong R.N. 2017: The effect of titanite crystallisation on Eu and Ce anomalies in zircon and its implications for the assessment of porphyry Cu deposit fertility. *Earth and Planetary Science Letters* 472, 107–119. https://doi.org/10.1016/j.epsl.2017.05.010

Ludwig K. 2003: User's manual for Isoplot 3.00: A geochronological toolkit for Microsoft Excel. *Berkeley Geochronology Center, Spec. Publ* 4a.

Maniar P.D. & Piccoli P.M. 1989: Tectonic discrimination of granitoids. *Geological Society of America Bulletin* 101, 635–643. https://doi.org/10.1130/0016-7606(1989)101%3C0635:TDOG%3E2.3.CO;2

Méheut M., Ibañez-Mejia M. & Tissot F.L. 2021: Drivers of zirconium isotope fractionation in Zr-bearing phases and melts: the roles of vibrational, nuclear field shift and diffusive effects. *Geochimica et Cosmochimica Acta* 292, 217–234. https://doi.org/10.1016/j.gca.2020.09.028

Metcalfe I. 2013: Gondwana dispersion and Asian accretion: Tectonic and palaeogeographic evolution of eastern Tethys. *Journal of Asian Earth Sciences* 66, 1–33. https://doi.org/10.1016/j.jseaes.2012.12.020

Miles A., Graham C., Hawkesworth C., Gillespie M., Hinton R. & Bromiley G. 2014: Apatite: A new redox proxy for silicic magmas? *Geochimica et Cosmochimica Acta* 132, 101–119. https://doi.org/10.1016/j.gca.2014.01.040

Moghadam H.S., Li X.H., Stern R.J., Santos J.F., Ghorbani G. & Pourmohsen M. 2016: Age and nature of 560–520 Ma calc-alkaline granitoids of Biarjmand, northeast Iran: insights into Cadomian arc magmatism in northern Gondwana. *International Geology Review* 58, 1492–1509. https://doi.org/10.1080/00206814.2016.1166461

Moghadam H.S., Li Q., Griffin W., Stern R., Ishizuka O., Henry H., Lucci F., O'Reilly S. & Ghorbani G. 2020: Repeated magmatic buildup and deep "hot zones" in continental evolution: The Cadomian crust of Iran. *Earth and Planetary Science Letters* 531, 115989. https://doi.org/10.1016/j.epsl.2019.115989

Moghaddam S.P., Salehi M.A., Jafarzadeh M. & Zohdi A. 2020: Provenance, palaeoweathering and tectonic setting of the Ediacaran Bayandor Formation in NW Iran: implications for the northern Gondwana continental margin during the late Neoproterozoic. *Journal of African Earth Sciences* 161, 103670. https://doi.org/10.1016/j.jafrearsci.2019.103670

Mollai H., Hashemi S.M. & Kardani Y. 2014: Geology and geochemistry of Yakhab Granodiorite, Yazd Province, East Central Iran, *Neues Jahrbuch für Geologie und Paleontologie-Abhandlungen*, 277–297. https://doi.org/10.1127/0077-7749/2014/0425

Mollai H., Dabiri R., Torshizian H.A., Pe-Piper G. & Wang W. 2019: Cadomian crust of Eastern Iran: evidence from the Tapeh Tagh granitic gneisses. *International Geology Review*, 1–21. https://doi.org/10.1080/00206814.2019.1670100

Nakamura N. 1974: Determination of REE, Ba, Fe, Mg, Na and K in carbonaceous and ordinary chondrites, *Geochimica et Cosmochimica Acta* 38, 757–775.

Narduzzi F., Farina F., Stevens G., Lana C. & Nalini Jr H. 2017: Magmatic garnet in the Cordilleran-type Galiléia granitoids of the Araçuaí belt (Brazil): Evidence for crystallization in the lower crust. *Lithos* 282, 82–97. https://doi.org/10.1016/j.lithos.2017.02.017

Newton R. & Haselton H. 1981: Thermodynamics of the garnet–plagioclase–Al_2SiO_5–quartz geobarometer. In: Thermodynamics of minerals and melts. *Springer*, 131-147

Newton R., Smith J. & Windley B. 1980: Carbonic metamorphism, granulites and crustal growth. *Nature* 288, 45–50. https://doi.org/10.1038/288045a0

Nouri F., Azizi H., Stern R.J., Asahara Y., Khodaparast S., Madanipour S. & Yamamoto K. 2018: Zircon U–Pb dating, geochemistry and evolution of the Late Eocene Saveh magmatic complex, central Iran: Partial melts of sub-continental lithospheric mantle and magmatic differentiation. *Lithos* 314, 274–292. https://doi.org/10.1016/j.lithos.2018.06.013

Nozaem R., Mohajjel M., Rossetti F., Della Seta M., Vignaroli G., Yassaghi A., Salvini F. & Eliassi M. 2013: Post-Neogene right-lateral strike–slip tectonics at the north-western edge of the Lut Block (Kuh-e–Sarhangi Fault), Central Iran. *Tectonophysics* 589, 220–233. https://doi.org/10.1016/j.tecto.2013.01.001

Nutman A.P., Mohajjel M., Bennett V.C. & Fergusson C.L. 2014: Gondwanan Eoarchean–Neoproterozoic ancient crustal material in Iran and Turkey: zircon U–Pb–Hf isotopic evidence. *Canadian Journal of Earth Sciences* 51, 272–285. https://doi.org/10.1139/cjes-2013-0138

Pankhurst R. & Pidgeon R. 1976: Inherited isotope systems and the source region pre-history of early Caledonian granites in the Dalradian Series of Scotland, *Earth and Planetary Science Letters* 31, 55–68. https://doi.org/10.1016/0012-821X(76)90096-0

Pearce J.A. 2008: Geochemical fingerprinting of oceanic basalts with applications to ophiolite classification and the search for Archean oceanic crust. *Lithos* 100, 14–48. https://doi.org/10.1016/j.lithos.2007.06.016

Pearce J.A., Harris N.B. & Tindle A.G. 1984: Trace element discrimination diagrams for the tectonic interpretation of granitic rocks, *Journal of Petrology* 25, 956–983. https://doi.org/10.1093/petrology/25.4.956

Pin C. & Paquette J.-L. 1997: A mantle-derived bimodal suite in the Hercynian Belt: Nd isotope and trace element evidence for a subduction-related rift origin of the Late Devonian Brévenne metavolcanics, Massif Central (France). *Contributions to Mineralogy and Petrology* 129, 222–238. https://doi.org/10.1007/s004100050334

Poursoltani M.R. & Hrati Sabzvar M. 2019: Porosity evolution and diagenetic history of the upper Jurassic Mozduran Formation, eastern Kopet-Dagh Basin, NE Iran. *Iranian Journal of Earth Sciences* 11, 141–159.

Pupin J. 1980: Zircon and granite petrology. *Contributions to Mineralogy and Petrology* 73, 207–220. https://doi.org/10.1007/BF00381441

Ramezani J. & Tucker R.D. 2003: The Saghand region, central Iran: U–Pb geochronology, petrogenesis and implications for Gondwana tectonics. *American Journal of Science* 303, 622–665. https://doi.org/10.2475/ajs.303.7.622

Romer R., Schneider J. & Linnemann U. 2010: Post-Variscan deformation and hydrothermal mineralization in Saxo-Thuringia and beyond: a geochronological review. In: Pre-Mesozoic geology of Saxo-Thuringia: from the Cadomian active margin to the Variscan Orogen. *Schweizerbart*, 347–360

Rong W., Zhang S.B., Zheng Y.F. & Gao P. 2018: Mixing of felsic magmas in granite petrogenesis: geochemical records of zircon and garnet in peraluminous granitoids from South China. *Journal of Geophysical Research: Solid Earth* 123, 2738–2769. https://doi.org/10.1002/2017JB014022

Ross P.-S. & Bédard J.H. 2009: Magmatic affinity of modern and ancient subalkaline volcanic rocks determined from trace-element discriminant diagrams. *Canadian Journal of Earth Sciences* 46, 823–839. https://doi.org/10.1139/E09-054

Rossetti F., Nozaem R., Lucci F., Vignaroli G., Gerdes A., Nasrabadi M. & Theye T. 2015: Tectonic setting and geochronology of the Cadomian (Ediacaran-Cambrian) magmatism in central Iran,

Kuh-e-Sarhangi region (NW Lut Block). *Journal of Asian Earth Sciences* 102, 24–44.

Ruttner A. & Nabavi M.H. 1970: Geological Map of the Ozbak Kuh Mountains 1:100.000. *Offset Press NCC*.

Saeidi H., Lashkaripour G. & Ghafoori M. 2020: Evaluation of land subsidence in Kashmar-Bardaskan plain, NE Iran. *Iranian Journal of Earth Sciences* 12, 280–291.

Samperton K.M., Schoene B., Cottle J.M., Keller C.B., Crowley J.L. & Schmitz M.D. 2015: Magma emplacement, differentiation and cooling in the middle crust: Integrated zircon geochronological–geochemical constraints from the Bergell Intrusion, Central Alps. *Chemical Geology* 417, 322–340. https://doi.org/10.1016/j.chemgeo.2015.10.024

Schaltegger U., Schmitt A. & Horstwood M. 2015: U–Th–Pb zircon geochronology by ID-TIMS, SIMS, and laser ablation ICP-MS: recipes, interpretations, and opportunities. *Chemical Geology* 402, 89–110. https://doi.org/10.1016/j.chemgeo.2015.02.028

Schmidt M.W. & Poli S. 2004: Magmatic epidote. *Reviews in Mineralogy and Geochemistry* 56, 399–430. https://doi.org/10.2138/gsrmg.56.1.399

Shahabpour J. 2007: Island-arc affinity of the central Iranian volcanic belt. *Journal of Asian Earth Sciences* 30, 652–665. https://doi.org/10.1016/j.jseaes.2007.02.004

Sheibi M., Esmaeily D., Nédélec A., Bouchez J.L. & Kananian A. 2010: Geochemistry and petrology of garnet-bearing S-type Shir-Kuh Granite, southwest Yazd, Central Iran. *Island Arc* 19, 292–312. https://doi.org/10.1111/j.1440-1738.2010.00707.x

Smythe D.J. & Brenan J.M. 2015: Cerium oxidation state in silicate melts: Combined fO_2, temperature and compositional effects. *Geochimica et Cosmochimica Acta* 170, 173–187. https://doi.org/10.1016/j.gca.2015.07.016

Soffel H., Schmidt S., Davoudzadeh M. & Rolf C. 1996: New palaeomagnetic data from Central Iran and a Triassic palaeoreconstruction. *Geologische Rundschau* 85, 293–302. https://doi.org/10.1007/BF02422235

Stern R.J. 1994: Arc assembly and continental collision in the Neoproterozoic East African Orogen: implications for the consolidation of Gondwanaland. *Annual Review of Earth and Planetary Sciences* 22, 319–351. https://doi.org/10.1146/annurev.ea.22.050194.001535

Stern R.J. 2008: Neoproterozoic crustal growth: the solid Earth system during a critical episode of Earth history. *Gondwana Research* 14, 33–50. https://doi.org/10.1016/j.gr.2007.08.006

Sun S.-S. & McDonough W.F. 1989: Chemical and isotopic systematics of oceanic basalts: implications for mantle composition and processes. *Geological Society, London, Special Publications* 42, 313–345. https://doi.org/10.1144/GSL.SP.1989.042.01.19

Szopa K., Gawęda A., Müller A. & Sikorska M. 2013: The petrogenesis of granitoid rocks unusually rich in apatite in the Western Tatra Mts.(S-Poland, Western Carpathians). *Mineralogy and Petrology* 107, 609–627. https://doi.org/10.1007/s00710-012-0262-2

Tadayon M., Rossetti F., Zattin M., Nozaem R., Calzolari G., Madanipour S. & Salvini F. 2017: The post-Eocene evolution of the Doruneh Fault region (central Iran): The intraplate response to the Reorganization of the Arabia-Eurasia collision zone. *Tectonics* 36, 3038–3064. https://doi.org/10.1002/2017TC004595

Tarabi S., Emami M.H., Modabberi S. & Sheikh Zakariaee S.J. 2019: Eocene-Oligocene volcanic units of Momen Abad, east of Iran: petrogenesis and magmatic evolution. *Iranian Journal of Earth Sciences* 11, 126–140.

Thompson J. & Hovis G. 1979: Structural-thermodynamic relations of the alkali feldspars. *Transactions of the American Crystallographic Association* 15, 1–26.

Watson E.B. & Harrison T.M. 1983: Zircon saturation revisited: temperature and composition effects in a variety of crustal magma types. *Earth and Planetary Science Letters* 64, 295–304. https://doi.org/10.1016/0012-821X(83)90211-X

White R., Powell R. & Johnson T. 2014: The effect of Mn on mineral stability in metapelites revisited: New a–x relations for manganese-bearing minerals. *Journal of Metamorphic Geology* 32, 809–828. https://doi.org/10.1111/jmg.12095

Xiao L., Xu Y., Mei H., Zheng Y., He B. & Pirajno F. 2004: Distinct mantle sources of low-Ti and high-Ti basalts from the western Emeishan large igneous province, SW China: implications for plume–lithosphere interaction. *Earth and Planetary Science Letters* 228, 525–546. https://doi.org/10.1016/j.epsl.2004.10.002

Xu Y., Chung S.-L., Jahn B.-m. & Wu G. 2001: Petrologic and geochemical constraints on the petrogenesis of Permian–Triassic Emeishan flood basalts in southwestern China. *Lithos* 58, 145–168. https://doi.org/10.1016/S0024-4937(01)00055-X

Yongsheng L., Zhaochu H., Keqing Z., Changgui G., Shan G., Juan X. & Haihong C. 2010: Reappraisement and refinement of zircon U-Pb isotope and trace element analyses by LA-ICP-MS. *Chinese Science Bulletin* 55, 1535–1546. https://doi.org/10.1007/s11434-010-3052-4

Zanchi A., Malaspina N., Zanchetta S., Berra F., Benciolini L., Bergomi M., Cavallo A., Javadi H.R. & Kouhpeyma M. 2015: The Cimmerian accretionary wedge of Anarak, Central Iran. *Journal of Asian Earth Sciences* 102, 45–72. https://doi.org/10.1016/j.jseaes.2014.08.030

Zen E.-a. 1985: Implications of magmatic epidote-bearing plutons on crystal evolution in the accreted terranes of northwestern North America. *Geology* 13, 266–269. https://doi.org/10.1130/0091-7613(1985)13%3C266:IOMEPO%3E2.0.CO;2

Zhang Z., Mahoney J.J., Mao J. & Wang F. 2006: Geochemistry of picritic and associated basalt flows of the western Emeishan flood basalt province, China. *Journal of Petrology* 47, 1997–2019. https://doi.org/10.1093/petrology/egl034

Ziemniak G., Kośmińska K., Petrík I., Janák M., Walczak K., Manecki M. & Majka J. 2019: Th–U–total Pb monazite geochronology records Ordovician (444 Ma) metamorphism/partial melting and Silurian (419 Ma) thrusting in the Kåfjord Nappe, Norwegian Arctic Caledonides. *Geologica Carpathica* 70, 494–511. https://doi.org/10.2478/geoca-2019-0029

Electronic Supplement S1 is available online at http://geologicacarpathica.com/data/files/supplements/GC-72-6-Mollai_Suppl_S1.xlsx